Improving Dust Aerosol Optical Depth (DAOD) Retrievals from GEOKOMPSAT-2A (GK-2A) Satellite for Daytime and Nighttime Monitoring

Soi Ahn , Hyeon-Su Kim , Jae-Young Byon * , Hancheol Lim

Posted Date: 18 December 2023

doi: 10.20944/preprints202312.1275.v1

Keywords: Dust Aerosol Optical Depth (DAOD); GK-2A; Thermal Infrared, Dust; Cumulative distribution function (CDF); Aerosol Robotic Network (AERONET)

Article

Improving Dust Aerosol Optical Depth (DAOD) Retrievals from GEOKOMPSAT-2A (GK-2A) Satellite for Daytime and Nighttime Monitoring

Soi Ahn [1], Hyeon-Su Kim [2], Jae-Young Byon [2,*] and Hancheol Lim [2]

[1] Environmental Satellite Center (ESC), National Institute of Environmental Research (NIER), 42, Hwangyeong-ro, Seo-gu, Incheon 22689, Korea; jjahn@korea.kr (S.A.)
[2] National Meteorological Satellite Center (NMSC); Korea Meteorological Administration (KMA), Jincheon-gun 27803, South Korea; atmos1305@korea.kr (H.-S.K.), hclim09@korea.kr (H.-C.L.)
* Correspondence: byonjy@kma.go.kr (J.-Y.B), Tel.: +82-070-7850-5903

Abstract: The Advanced Meteorological Image (AMI) onboard GEOKOMPSAT 2A (GK-2A) enables the retrieval of dust aerosol optical depth (DAOD) from geostationary satellites using infrared (IR) channels. IR observations allow the retrieval of DAOD and the dust layer altitude (24 hour) over surface properties, particularly over deserts. In this study, dust events in northeast Asia from 2020 to 2021 were investigated using five GK-2A thermal IR bands (8.7, 10.5, 11.4, 12.3, and 13.3 μm). For the dust cloud, the observed brightness temperature differences (BTDs) of 10.5 and 12.3 μm were found to be always negative, while the BTD of 8.7 and 10.5 μm varies relying on the dust intensity. Making the best use of optical properties, a physical approach for DAOD lookup tables (LUTs) was developed using IR channels to retrieve the DAOD. This study simulated the characteristics of thermal radiation transfer using the forward model and dust aerosols can explain by BTD (10.5, 12.3 μm), which is an intrinsic characteristic of dust aerosol. The DAOD and property of dust can be gained from the brightness temperature (BT) of 10.5 μm and the BTD of 10.5, 12.3 μm. Additionally, the cumulative distribution function (CDF) was employed to strengthen the continuity of 24-hour DAOD, which was applied to the algorithm by calculating the conversion value coefficient for the DAOD error correction of the IR with daytime visible aerosol optical depth (VAOD) as the true value. The results show that DAOD product can be successfully used during both daytime and nighttime to continuously monitor the flow of yellow dust from the GK-2A satellite in northeast Asia. In particular, the validation result of IR DAOD was similar to that of the active satellite product (CALIPSO/CALIOP), which showed a tendency similar to that for IR DAOD at night.

Keywords: dust aerosol optical depth (DAOD); GK-2A; thermal infrared; dust; cumulative distribution function (CDF); aerosol robotic network (AERONET)

1. Introduction

We are currently more aware of the environmental challenges in our present and future. One important aspect is to comprehend the place of atmospheric aerosols in various meteorological processes across different environment, impacting climate, weather, and air quality. Aerosol particles are thought to play a crucial role in visibility [1,2], dimming [3], precipitation [4], air quality [5], and even human health, influencing aspects like blood circulation [6].

Mineral dust aerosols are crucial part of the atmosphere. Dust cause variabilities such as interaction with clouds by acting, optical properties of clouds, thereby influencing the radiative budget and having a global climate change such as abnormal weather.

In northeast Asia, the moving with the wind of aerosols relies on meteorological conditions and affects the air quality of areas. In particular, dust storms occur frequently during the springtime and cause poor air quality in northeast Asia. In recent years, the frequency of yellow dust events is increasing in the winter and fall seasons, as they have become drier due to climate change. Therefore, an essential parameter for comprehension the Earth's climate circulation system.

 doi:10.20944/preprints202312.1275.v1

Satellite monitoring is an important implement for scrutinizing the aerosol flow, properties, type such as mineral dust, fine particles, volcanic ash. The aerosol optical depth (AOD) retrieved from satellites is the best ordinarily utilized indirect measurement for atmospheric environmental research, modeling studies; however, many researchers are putting a lot of effort into reducing errors and deriving accurate AOD [7]. Many ground-based remote-sensing aerosol networks, such as the aerosol robotic network (AERONET), have been set up global. Additionally, the basic optical properties are derived from many Earth observation satellites, such as Geosynchronous Earth Orbit (GEO) satellites, including the Advanced Baseline Imager (ABI), Advanced Himawari Imager (AHI), Advanced Meteorological Imager (AMI), and Geostationary Ocean Color Imager (GOCI). Furthermore, aerosol retrieval algorithms have been developed for Low Earth Orbit (LEO) satellite instruments such as the Advanced Very High-Resolution Radiometer (AVHRR) [8,9], Ozone Monitoring Instrument (OMI) [10], Multiangle Imaging Spectro-Radiometer (MISR) [11], Moderate Resolution Imaging Spectrometer (MODIS) [12], Visible Infrared Imaging Radiometer Suite (VIIRS) [13,14], and Cloud and Aerosol Imager (CAI) [15].

Previously, many studies on aerosol detected by satellite mainly measured the visible channel. Currently, GEO and LEO satellites have various visible and near-IR channels, which enable corrected reflectivity and aerosol property retrieval with high accuracy. However, aerosol observations using the visible channel were limited to the day; therefore, it was difficult to determine the aerosol flow at night. Therefore, we attempted to study dust aerosol in the nighttime IR spectral domain, such as the Atmospheric Infrared Sounder (AIRS) or Infrared Atmospheric Sounding Interferometer (IASI) [16,17]. IR spectral observations are necessary to complement the solar measurements. First, it is momentous to decide the terrestrial radiative forcing due to the effect of dust on IR radiation [18]. Excluding the bright surfaces such as snow, deserts, it is important to accurately observe the absorption of longwave radiation emitted from the Earth's surface [19]. Second, it reacts sensitively depending on the size of aerosol particle. For example, coarse mode such as mineral aerosols are observe in the IR domain, on the other hand pollution are derived in both the visible and IR domain, making it difficult to discriminate them. Third, IR observations can be observed at night, allowing the flow of dust to be monitored, and have proven to be practical in acquiring aerosols regardless of surface characteristics [20–23]. Therefore, the objectives of this study were to advance a DAOD algorithm to identify dust-storm outbreaks and their spatial extent using IR channels from Geo-Kompsat 2A (GK-2A). Since only IR channels were used, the algorithm was applicable to both daytime and nighttime conditions. DAOD of IR domain was derived using a physical method based on offline calculated look-up tables (LUTs). Furthermore, to increase the accuracy of the developed DAOD, the CDF method was applied to analyze its qualitative and quantitative performances. This generalized approach is summarized in Section 2, and the results and discussion of the validation of the DAOD against AERONET and CALIPSO within the period of a dust event in 2021 are described in Section 3; the summary and conclusions of the study are given in Section 4.

2. Materials and Methods

2.1. Materials

2.1.1. Satellite observations: GEOKOMPSAT-2A (GK-2A)

The GK-2A of Korean Meteorological Administration (KMA) has been performing a meteorological satellite mission since December 5, 2018 and is currently operating well. GK-2A life is 10 years during the 8 months in-orbit test period, the capability with multi-band and high temporal and spatial resolution was verified. Currently, GK-2A AMI observes the 10 min on full disk and 2 min over the Korean Peninsula using the high spatiotemporal resolution (0.5–2 km). GK-2A has 16 channels which a visual channel (0.47, 0.51, 0.64, and 0.86 μm), a near-IR channel (1.38 and 1.61 μm), and an IR channel (3.8, 6.3, 6.9, 7.3, 8.7, 9.6, 10.5, 11.2, 12.3, and 13.3 μm) (Table 1), similar to the GOES-16 (United States) and Himawari-8 (Japan). This satellite not only greatly improve the accuracy of precision weather and prognosticating extreme weather over the Korean Peninsula and the Asia-

 doi:10.20944/preprints202312.1275.v1

Pacific region. GK-2A AMI diversifies channels and provides RGB color images using compositing techniques. This allows real-time monitoring of various weather phenomena. In addition, it can be used for unpredictable and dangerous weather through continuous observation.

Table 1. Summary of the GK-2A/AMI spectral bands.

Bands	Band Name	Wavelength		Band Width (Max)	Spatial Resolution (km)
		Min (um)	Max (um)		
1 (blue)	VIS0.47	0.43	0.48	0.075	1
2 (green)	VIS0.51	0.52	0.52	0.063	1
3 (red)	VIS0.64	0.63	0.66	0.125	0.5
4 (VIS)	VIS0.86	0.85	0.87	0.088	1
5 (NIR)	NIR1.37	1.37	1.38	0.03	2
6 (NIR)	NIR1.61	1.60	1.62	0.075	2
7 (IR)	SWIR3.8	3.74	3.96	0.5	2
8 (IR)	WV6.3	6.06	6.43	1.038	2
9 (IR)	WV6.9	6.89	7.01	0.5	2
10 (IR)	WV7.3	7.26	7.43	0.688	2
11 (IR)	IR8.7	8.44	8.76	0.5	2
12 (IR)	IR9.6	9.54	9.72	0.475	2
13 (IR)	IR10.5	10.3	10.6	0.875	2
14 (IR)	IR11.2	11.1	11.3	1.0	2
15 (IR)	IR12.3	12.2	12.5	1.25	2
16 (IR)	IR13.3	13.2	13.4	0.75	2

2.1.2. AERONET

The Aerosol Robotic Network (AERONET) is an international ground-based aerosol remote sensing network [24] (https://aeronet.gsfc.nasa.gov/). It is used as representative data to validate aerosol product from satellite. AERONET AOD uncertainty at Level 2 (version 2), is approximately 0.01 to 0.02, which can be comprehended as a true value to validate AMI AOD over land and ocean. In this study, AERONET data was used to validate the accuracy of DAOD by performing a spatiotemporal collocation between AMI AOD 11.4 μm and AERONET observations. AERONET observations within a 10-min time range were averaged to perform ground-measured aerosol loading, and averaged AMI 11.4 μm AODs within a 10-km radius of one AERONET site were used to represent satellite aerosol movement.

2.1.3. Suomi-NPP/VIIRS

The Visible Infrared Imaging Radiometer Suite (VIIRS) instrument aboard the Suomi National Polar-Orbiting Partnership (S-NPP) satellite was launched in October 2011 and was extend the performance of MODIS. VIIRS has various channel (visible, short, IR spectral) and provide a variety of products and have precise accuracy [25]. In particular, VIIRS aerosol data (VIIRS AOD550s at Intermediate Product level) was computed in pixel mode with a spatial resolution of 0.75 km, unlike MODIS, it is advantageous to validate an accuracy of the product with high spatial resolution. VIIRS product was used and downloaded from the National Oceanic and Atmospheric Administration's (NOAA)'s Comprehensive Large Array-Data Stewardship System (CLASS) (http://www.class.ncdc.noaa.gov/saa/products/welcom). The product has undertaken continuous evaluations with an uncertainty range: [$\Delta\tau = -0.470\tau - 0.01$ (lower bound), $-0.0058\tau + 0.09$ (upper bound)] over land and [$\Delta\tau = -0.238\tau + 0.01$ (lower bound), $0.194\tau + 0.048$ (upper bound)] over ocean [13]. The VIIRS aerosol product used to verify the accuracy of the DAOD developed in this study for the yellow sand period in 2020.

Preprints (www.preprints.org) | NOT PEER-REVIEWED | Posted: 18 December 2023 doi:10.20944/preprints202312.1275.v1

2.1.4. CALIPSO/CALIOP

The Cloud-Aerosol Lidar with Orthogonal Polarization (CALIOP), the main instrument of Cloud-Aerosol Lidar and Infrared Pathfinder Satellite Observation (CALIPSO) spacecraft is a major sensor that studies interaction between aerosol and clous, and vertical profiles. Particularly, CALIPSO derives profiles of attenuated backscatter at 532 and 1064 nm and polarized backscatter at 532 nm. This study was used active sensor, it can retrieve information about aerosols and clous both during the daytime and nighttime. Also, CALIPSO has high horizontal and vertical resolutions of 333 m and 30−60 m, respectively, it pivotal for comprehension the aerosol (e.g., aerosol type, extinction profile, height, optical depth), and clouds of property [26,27]. CALIPSO has three level products, which used raw signals to distinguish cloud and aerosols (L1), reclassifies the types (L2), and then provides specific variable such as extinction coefficients, AOD (L3). In this study, we used the L3 to validate DAOD at night when yellow dust occurred.

2.1.5. Dust storm events in 2020–2021

In this study, the dust storm events that occurred between 2020 and 2021 in Northeast Asia were focused on because GK-2A satellite data are available for 24 h, especially using the visible and IR channels of the retrieved DAOD. Therefore, the National Meteorological Satellite Center (NMSC) of KMA provides information on the optical depth monitoring of yellow dust while simultaneously identifying the flow of dust storms and selecting cases that affect the Korean Peninsula for use in forecasting (Table 2). This was applied to the dust event that occurred in the spring of 2021 using training data based on the case of a dust storm in 2020.

Table 2. Dust events in 2020–2021 used this study.

satellite data composition	Dust event date	Oriented dust place	Anylsis Day
Training Dataset Dust Episodes (2020)	February 16–17, 2020	Dalian (Northeast of China)	00:00 UTC–10:50 UTC
	February 20–23, 2020	Wulatezhongqi/Yanan~ Shandong province/ Bohai sea	
	March 12–14, 2020	Tibetan Plateau~ Shandong province~ Bohai sea	
	March 18–19, 2020	Inner Mongolia~Bohai sea	
	March 30–April 2, 2020	Southeast of Mongolia	
	April 3–7, 2020	Wulatezhongqi (East of Monolia)	
	April 15–18, 2020	Mongolia	
	April 20–22, 2020	Dandong~Bohai sea~ Tongliao, Siping	
	April 24–25, 2020	East of Mongolia	
	May 10–11, 2020	Bohia sea~Siping	
	May 11–14, 2020	Inner Mongolia	
	May 31–June 6, 2020	Gobi Desert~ Wulatezhongqi~ Erenhot~Jurihe	
	June 5–11, 2020	Taklamakan	
	June 9 June–11, 2020	Gobi Desert	
	October 19–23, 2020	Gobi Desert	

Preprints (www.preprints.org) | NOT PEER-REVIEWED | Posted: 18 December 2023 doi:10.20944/preprints202312.1275.v1

	October 30–November 2, 2020	Gobi Desert	
	November 5–8, 2020	Gobi Desert	
	November 7–8, 2020	Manchuria	
Analysis Dataset Dust Edpisodes (2021)	January 13–14, 2021	Gobi Desert	00:00 UTC–23:50 UTC
	February 21–22, 2021	Gobi Desert	
	March 15–17, 2021	Mongolia	
	March 23–28, 2021	Gobi Desert	
	April 15–17, 2021	Mongolia	
	April 26–27, 2021	Mongolia	
	May 04–07, 2021	Gobi Desert	
	May 23–24, 2021	Gobi Desert	
	December 16, 2021	Inner Mongolia	

2.2. Methods

2.2.1. Look-up-table-based physical retrieval algorithm

The goal was to retrieve the DAOD during the day and night by utilizing a GK-2A IR channel. A flowchart of the DAOD automated algorithm is shown in Figure 1.

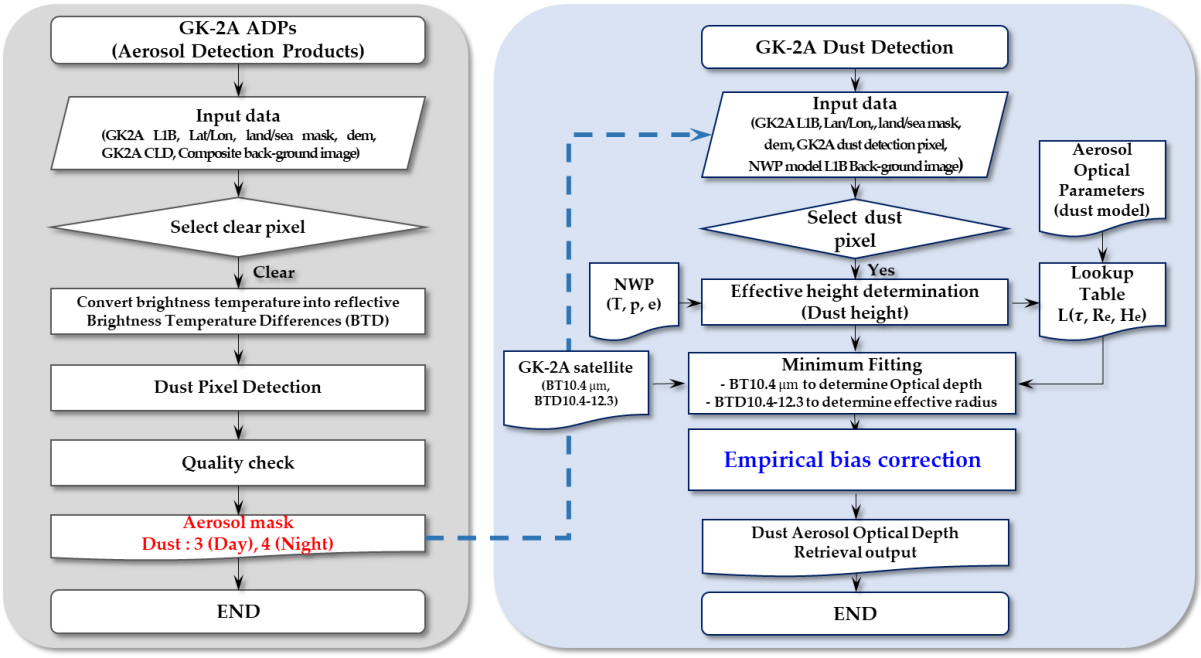

Figure 1. Flowchart of the Dust Aerosol Optical Depth (DAOD) product algorithm used by GK-2A/AMI.

2.2.1.1. GK-2A dust pixel retrievals

The GK-2A AMI Aerosol Detection Products (ADPS) algorithm can monitor aerosol category (e.g., dust, haze, and volcanic ash) fusing the multiple channels [28,29]. These characterizations and physical principles were used to determine the threshold values of the dust algorithm. A GK-2A ADPS algorithm based on the BTD method was developed for the retrieval of aerosol types and to reflect daytime, nighttime land, and ocean characteristics differently. This study focused on dust pixels using thermal IR (TIR) channels. The TIR-based method is widely used because of its advantage of monitoring dust at night and over bright surfaces, such as deserts. Assuming that the temperature most similar to the surface temperature was a clear pixel, the boundary value of $BT_{10.5}$

Preprints (www.preprints.org) | NOT PEER-REVIEWED | Posted: 18 December 2023 doi:10.20944/preprints202312.1275.v1

was used as the most basic value [30]. During the day, $BT_{10.5}$ decreases in the presence of dust due to the maximum dust absorption in 10.5 μm [31], while it is the highest in bright surface (Equations (1), common use of land and ocean).

$$BT_{10.5} > 243.0\ K \quad (1)$$

The boundary value of this dust mask relies on the spatial and thermal distinctions between aerosols and clouds and the depression of the brightness temperature difference (BTD) between $BT_{10.5}$ and $BT_{12.3}$ ($BTD_{10.5-12.3}$, Equations (2)) can be exhibited by the dust plumes [31–35]. Using the characteristic of preferentially absorbing shorter wavelengths, cloud components with silicate particles can be discriminated using various IR bands [36]. Silicate particles cause a negative BTD between $BT_{10.5}$ and $BT_{12.3}$ for the dust region, with the longer wavelength channel recording a higher brightness temperature [36]. $BT_{8.7}$ is not as affected by the presence of dust, but it was much lower than $BT_{10.5}$ under unspoiled sky conditions. Therefore, $BT_{8.7}$ and $BT_{10.5}$ ($BTD_{8.7-10.5}$, Equations (3)) are larger for dust than for the ground and clouds [31,37–40]. To improve the accuracy of dust detection, 11.2 μm and 12.3 μm ($BTD_{11.2-12.3}$, Equations (4)) have similar spectral characteristics, but have strong signals for weak or low-altitude dust [41]. The brightness temperature ratio (BTR) between the two wavelength channels was built on discriminate between the dust and surface property more exactly [42]. Usually, the ratios of $BT_{10.5}$ and $BT_{12.3}$ ($BTR_{10.5-12.3}$) values are lower than one over the dust region; therefore, in the algorithm, the boundary value was applied to increase the accuracy of dust detection (Equation 5). Furthermore, the BTR value was applied by changing the channel values $BT_{10.5}$ and $BT_{8.7}$ ($BTR_{10.5-8.7}$, Equation (6)). The BTD-BBTD (background) test uses 30-day background image data; therefore, it corrects the water vapor (Equation 7). D*-parameter (Equation (8)) is computed by combining the dust absorption rate difference of 8.7, 10.5, and 12.3 μm and the coefficient based on the empirical equation, and is a representative variable that can identify yellow dust. This parameter was created by Hansell detected nighttime dust, since many silicate minerals that have strong bands often absorb more at 8.7 μm than at 10.5 μm, leading to a negative $BTD_{8.7-10.5}$. Therefore, a parameter is often designed such that a value greater than one indicates dust, and a value lower than one indicates clouds [43].

On land (Equations (2)−(8)),

$$BT_{10.5} - BT_{12.3} \leq 0.1 \quad (2)$$

$$BT_{10.5} - BT_{8.7} < -0.8 \quad (3)$$

$$BT_{11.2} - BT_{10.5} \geq 0.5 \quad (4)$$

$$\text{Ratio}\left[\frac{BT_{10.5}}{BT_{12.3}}\right] \leq 0.1 \quad (5)$$

$$\text{Ratio}\left[\frac{BT_{10.5}}{BT_{8.7}}\right] \leq 0.1 \quad (6)$$

$$(BTD_{10.5-12.3}) - (BBTD_{10.5-12.3}) \quad (7)$$

$$D^* = exp\{[(BTD_{10.5-12.3}) - C] / [(BTD_{8.7-10.5}) - E]\} \quad (8)$$

where the offsets C and E were set to be -0.5 and 15.

In the ocean (Equations (9)−(15)),

$$BT_{10.5} - BT_{12.3} \leq 0.1 \quad (9)$$

$$BT_{10.5} - BT_{8.7} < -0.8 \quad (10)$$

$$BT_{11.2} - BT_{10.5} \geq 0.5 \quad (11)$$

Preprints (www.preprints.org) | NOT PEER-REVIEWED | Posted: 18 December 2023 doi:10.20944/preprints202312.1275.v1

$$\text{Ratio}\left[\frac{BT_{10.5}}{BT_{12.3}}\right] \leq 0.1 \tag{12}$$

$$\text{Ratio}\left[\frac{BT_{10.5}}{BT_{8.7}}\right] \leq 0.1 \tag{13}$$

$$(BTD_{10.5-12.3}) - (BBTD_{10.5-12.3}) \tag{14}$$

$$D^* = exp\{[(BTD_{10.5-12.3}) - C] \,/\, [(BTD_{8.7-10.5}) - E]\} \tag{15}$$

In this study, the DAOD using IR channels was calculated using only the dust pixels identified through the threshold test.

2.2.1.2. Forward simulation

After that dust characteristics of the BT and BTD (10.5 and 12.3 μm), should be selected an appropriate aerosol model. Dust aerosol model must be developed considering the complex refractive index, particle size distribution, and particle shape. Complex refractive index (RI) is a parameter that defines the interaction between electromagnetic radiation and matter [44]. The real part indicates the scattering properties and the imaginary part declares the absorption properties of the dust aerosol (Equation 16).

$$\text{Refractive Index}(\text{RI}, \lambda) = n(\lambda) - ik(\lambda) \tag{16}$$

where λ = wavelength, n = real part, and k = imagery part [45,46]

The particle size distribution is expressed as a lognormal distribution. During yellow dust, large particles become principal, and the lognormal distribution was selected as follows:

$$\frac{dv}{d\ln r} = \frac{C_{fine}}{\sqrt{2\pi}S_{fine}} \exp\left[-\frac{(\ln r - \ln r_{fine})^2}{2(S_{fine})^2}\right] + \frac{C_{coarse}}{\sqrt{2\pi}S_{coarse}} \exp\left[-\frac{(\ln r - \ln r_{coarse})^2}{2(S_{coarse})^2}\right] \tag{17}$$

where $dv/dlnr$ is the particle number size distribution; C_{fine} and C_{coarse} are the number of particles per cross-section of the atmospheric column (m^{-2}); r is the particle radius; r_{fine} and r_{coarse} are the modal radii; and S_{fine}, S_{coarse} are the standard deviations of $\ln r_{fine}$ and $\ln r_{coarse}$, respectively.

The shape of aerosol particles is difficult to define owing to their irregular shape and non-uniform size; therefore, the particles were assumed to be spherical in this study. The phase function can be expressed as follows:

$$\text{P}(\lambda, \theta) = \int_{r=0}^{r=\infty} \pi r^2 F(\lambda, r, RI, \theta) \frac{dN}{dlnr} dlnr \tag{18}$$

where F is the top of the atmosphere (TOA) radiative forcing in W/m^2; N is the particle number density; and r is the particle radius.

DISORT is a discrete ordinate radiative transfer program for sorting the radiative transfer equation [47]. The simulated the IR radiative transfer of the dust layer using previously calculated parameters (i.e., complex refractive index, particle size distribution, shape), and derived the values for the single scattering albedo (ω_0), asymmetry factor (g), extinction coefficient ratio (k). These calculated parameters together with a given optical depth of the dust layer, can be input the radiation transfer model, DISORT to simulate observations for IR wavelengths (Figure 2).

$$\text{Extinction Coefficient: } \sigma_{ext}(\lambda) = \sigma_{sca}(\lambda) + \sigma_{abs}(\lambda) \tag{19}$$

$$\text{Single Scattering Albedo: } \omega_0(\lambda) = \frac{\sigma_{sca}(\lambda)}{\sigma_{ext}(\lambda)} \tag{20}$$

$$\text{Asymmetry Factor g}(\lambda) = \frac{\int cos\theta P(\lambda, \theta) dcos(\theta)}{\int (\lambda, \theta) dcos(\theta)} \tag{21}$$

Preprints (www.preprints.org) | NOT PEER-REVIEWED | Posted: 18 December 2023 doi:10.20944/preprints202312.1275.v1

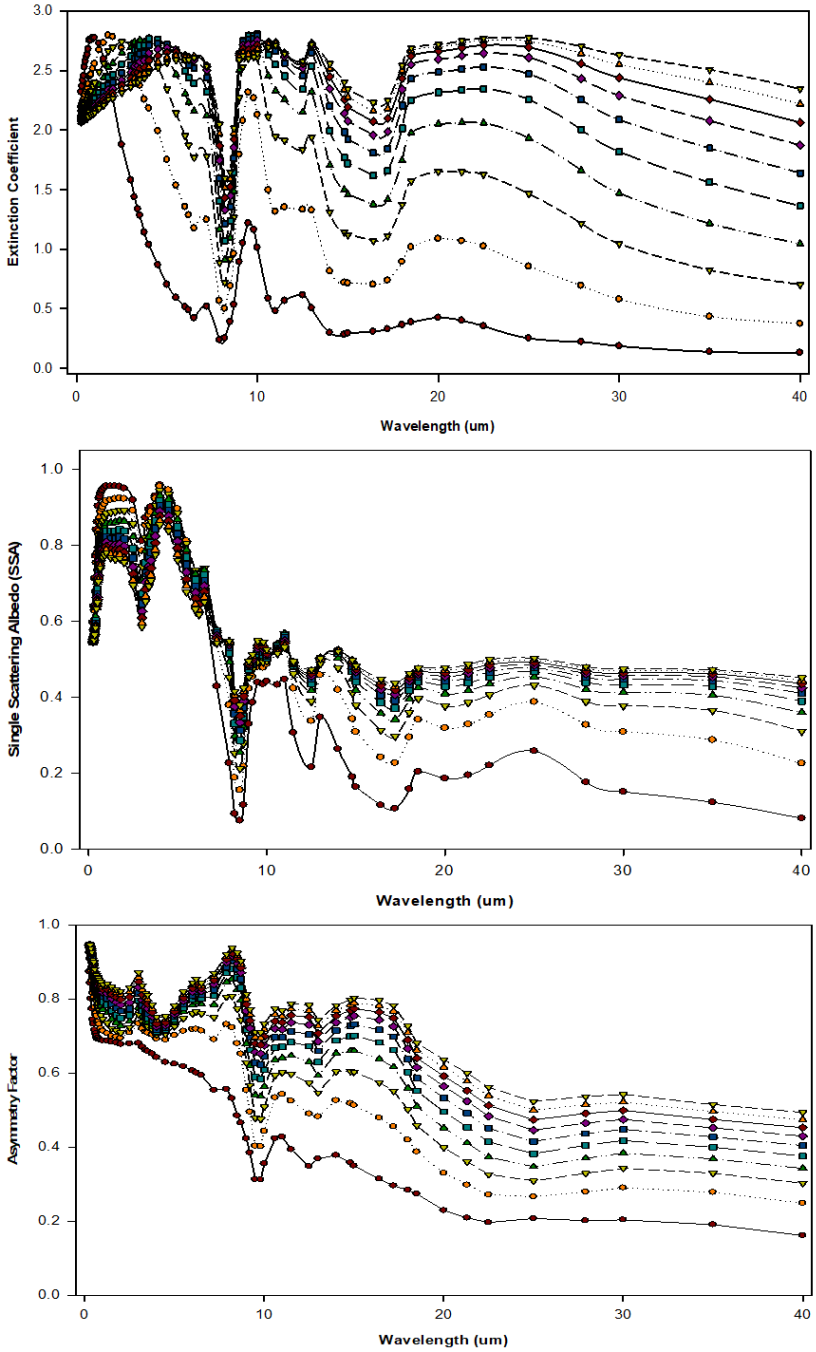

Figure 2. Simulation model results based on infrared channel characteristics by DISORT.

2.2.1.3. DAOD look-up table

Basically, the forward radiative transfer model in IR channels is as follows:

$$I_{TOA} = \epsilon_c I_{ac} + T_{ac}\epsilon_c B(T_c) + I_{clr}(1-\epsilon_c) \quad (22)$$

where I_{TOA} is the satellite-received radiance; I_{ac} is the radiance contribution from the region above the dust cloud; I_{clr} is the clear-sky radiance; T_{ac} represents the above-dust cloud transmission; T_c is the effective top temperature of dust layer; B operator is the Planck function; and (ϵ_c) is the emissivity at the top of the dust layer.

The cloud is defined by its cloud top temperature T_c and its emissivity ϵ_c. In equation (22), the transmission from the dust layer, dust cloud top temperature, and Planck function are related to dust extinction at IR wavelengths. By removing other terms, the DAOD can be derived analytically.

Preprints (www.preprints.org) | NOT PEER-REVIEWED | Posted: 18 December 2023 doi:10.20944/preprints202312.1275.v1

However, surface and dust cloud emissivity are relatively ambiguous, and the dust optical values were retrieved using LUTs calculated by radiative transfer [48]. The retrieval strategy was based on a physical approach that relied on the use of LUTs for the simulated DAOD (Table 3). In order to derive accurate DAOD, the measured top-of-atmosphere (TOA) radiance is a crucial key to computing the LUT using an appropriate aerosol dust model. TOA radiance was calculated using the Santa Barbara discrete ordinate radiative transfer (SBDART) (http://libradtran.org) [49].

Table 3. List of the input variables used for the calculation of the Dust Aerosol Optical Depth (DAOD) Lookup table.

Variable Name	Number of Entries	Entries
Wavelength	5	3.8, 10.5, 11.2, 12.4, 13.3 μm (considering spectral response function)
Solar zenith angle	9	0, 10, 20,30, ..., 80 (10 intervals)
Satellite zenith angle	17	0, 5, 10,15, ..., 80 (5 intervals)
Relative azimuth angle	18	0, 10, 20, ...,170 (10 intervals)
AOD	10	0.0, 0.3, 0.6, 0.9, 1.2, 1.5, 2.0, 3.0, 4.0, 5.0
Dust Aerosol model	10	1,2,3,4,5,6,7,8,9,10 μm (considering effective radius)
Dust Altitude	10	1,2,3,4,5,6,7,8,9,10 km

2.2.1.4. Estimation of the effective dust height

This study assumed a method using the GOES-R volcanic ash height, and it was the same in that it used height. [50]. This was assumed to be similar to inferring the height of volcanic ash by searching a temperature close to the height when volcanic ash moves. The retrieved T_{eff} was used to approximate the dust height and fine the closest matching temperature point and the linear interpolation weights and points were decided by finding T_{eff} within the Numerical Weather Prediction (NWP) temperature profile. In this study, the vertical NWP profiles utilized to dust retrieval was assigned a temperature that reflects the levels between the surface and the model tropopause height (approximately 10 km). Afterwards, the dust height was computed using the interpolation method (Equation 23).

$$H_{Dust}(height) = H_1 + \frac{T_{eff} - T_1}{T_2 - T_1}(H_2 - H_1) \quad (23)$$

where H_{Dust} is the dust height; T_1 and T_2 are the temperatures within the profile that bound T_{eff}, with T_1 is the temperature at the highest bounding level; and H_1 and H_2 are the dust heights of the bounding temperatures corresponding to T_1 and T_2, respectively [50].

From the forward simulation, it was viable to develop using temperature-difference model according to height (H_{Dust}). The temperature difference model includes $BT_{10.5}$ and $BTD_{10.5-12.3}$. The $BT_{10.5}$ and $BTD_{10.5-12.3}$ values calculated from the LUTs (simulated BT) were compared with the $BT_{10.5}$ and $BTD_{10.5-12.3}$ values calculated from the satellite (observed BT). $BT_{10.5}$ is highly correlated with dust optical depth and $BTD_{10.5-12.3}$ is nearby corresponded to particle volume [44]. The value with the minimum root-mean-square deviation (RMSD) is determined through comparison (Equation 24), and the optical depth and particle effective radii of the dust can be gained at the same time. Therefore, the accuracy of T_{ac} and T_c determines the reliability of the retrieved results (Figure 3).

$$\text{Min RMSD} = \frac{1}{N}\sqrt{\frac{(BT_{10.5(calc)} - BT_{10.5(obs)})^2}{BT_{10.5(obs)}}} + \frac{1}{N}\sqrt{\frac{(BTD_{10.5-12.3(calc)} - BTD_{10.5-12.3(obs)})^2}{BTD_{10.5-12.3(obs)}}} \quad (24)$$

Preprints (www.preprints.org) | NOT PEER-REVIEWED | Posted: 18 December 2023 doi:10.20944/preprints202312.1275.v1

where $BT_{10.5(calc)}$ is the BT calculated using the radiative transfer model; $BT_{10.5(obs)}$ is the GK2A satellite-observed BT; $BTD_{10.5-12.3(calc)}$ is the difference between the $BT_{10.5}$ and $BT_{12.3}$ using the radiative transfer model; and $BTD_{10.5-12.3(obs)}$ is the satellite-observed BTD.

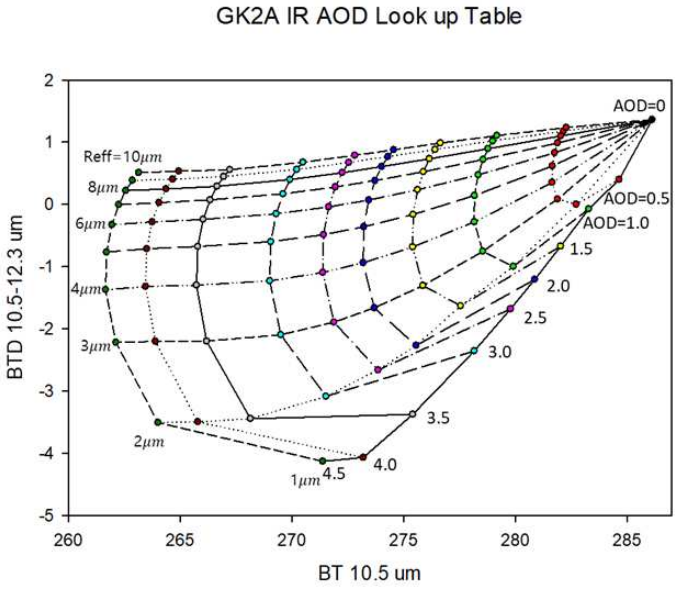

Figure 3. Example of the look-up table calculated according to the variation in optical depth and effective radii of dust particles.

2.2.2. Empirical bias correction method

Once the source of the empirical bias correction in the GK-2A DAOD has been recognized, the next stage was to progress an algorithm to correct it. In addition, to make a 24-hour continuous forecast, the DAOD concentration was corrected by comparing it with the DAOD of the visible channel. Specially, the CDF were used to adjust GK-2A satellite IR (10.5 μm) AOD in accordance with visible AOD. This method is particularly convenient for harmonizing and facilitating the information gained from difference source [51]. The difference is that, instead of converting the wavelength, it is converted into an empirical bias correction method using the value of the wavelength. The visible AOD of the GK-2A satellite has an accuracy of (RMSE =0.21, bias = 0.08 in 2020) and is being serviced and used for daytime monitoring. It is meaningful to use accuracy to correct the IR AOD.

$$DAOD\ (0 < DAOD < 1.6) = a_0 + a_1 DAOD + a_2 DAOD^2 + a_3 DAOD^3 \quad (25)$$

$$DAOD\ (1.6 \leq DAOD < 4) = a_4 + a_5 DAOD + a_6 DAOD^2 + a_7 DAOD^3 \quad (26)$$

where the regression coefficients $a_0 = 0.083$; $a_1 = -0.171$; $a_2 = 1.174$; $a_3 = -0.348$ ($0 < \text{DAOD} < 1.6$); $a_4 = -0.977$; $a_5 = 2.505$; $a_6 = -0.615$; and $a_7 = 0.075$ ($1.6 \leq \text{DAOD} < 4$) are gained through the fitting procedure, and new DAOD were computed and selectively applied according to the value of DAOD.

3. Results and Discussion

3.1. Dust detection using infrared channels from GK-2A

3.1.1. Comparisons of dust imagery products during the nighttime

To monitor the DAOD for 24 hours, accurately detecting dust at night using IR channels is essential. For qualitative evaluation at nighttime, the dust red green blue (RGB) imagery from the GK-2A/AMI (developed by the KMA NMSC) was used. This imagery was developed by selecting an appropriate channel to detect dust and converting it to R (11.2–10.5 $\boldsymbol{\mu m}$), G (10.5–8.7 $\boldsymbol{\mu m}$), B (10.5–

 doi:10.20944/preprints202312.1275.v1

13.3 $\boldsymbol{\mu m}$) using the BTD in the IR channel to monitor the occurrence and movement of dust. The images make it easier to visually discriminate between dust (purple-pink) and non-dust (green), enabling the identification of the type of cloud. On April 24, 2020, at 03:00 UTC (12:00 KST), a dust storm originated east of Mongolia and northern China and moved to the southeastern regions due to northwesterly winds (Figure 4). A high concentration of 407 $\boldsymbol{\mu g/m^3}$ was observed in Huimin, which affected a weak intensity of less than 200 $\boldsymbol{\mu g/m^3}$ at 21:00 UTC (April 25, 2020, at 05:00 KST). Afterwards, the storm began to affect the yellow sea at 22:00 UTC (April 25, 2020, at 07:00 KST) and penetrated into the Korean Peninsula at a concentration of 100–200 $\boldsymbol{\mu g/m^3}$ at 00:00 UTC (09:00 KST) on April 25. As a result of the GK-2A aerosol detection product analysis, this image shows that dust originated, entered the Shandon Peninsula, and moved to the southwest well on April 24, 2020, at 07:00 UTC–10:00 UTC (Figure 4a,b). Additionally, based on the yellow dust well, the darker the color, the stronger the dust storm. At 13:00 UTC (22:00 KST), dust was detected in the Yellow Sea, which moved southwest with a constant intensity (Figure 4c). When dust approached the ocean, it was continuously detected without discontinuity between land and sea, even though in many cases, dust detection was not possible because of the weakening of the detection strength due to the contrasting surface properties. Moreover, when dust occurs in clouds, it is important to prevent dust removal by clouds to increase the accuracy of dust detection. Therefore, yellow dust was not removed by the clouds, and it was continuously detected at 16:00 UTC–19:00 UTC (Figure 4d,e). GK-2A dust RGB showed a strong dust signal (pink) in northwest China and a weak dust signal (pale pink) in the vicinity of the Shandong Peninsula and the east sea of the Korean Peninsula. As a result of the qualitative comparison with GK-2A dust RGB, it appeared similar to the comparative GK-2A aerosol detection image, as it was detected using a strict threshold test and fewer pixels in the GK-2A dust RGB.

Preprints (www.preprints.org) | NOT PEER-REVIEWED | Posted: 18 December 2023 doi:10.20944/preprints202312.1275.v1

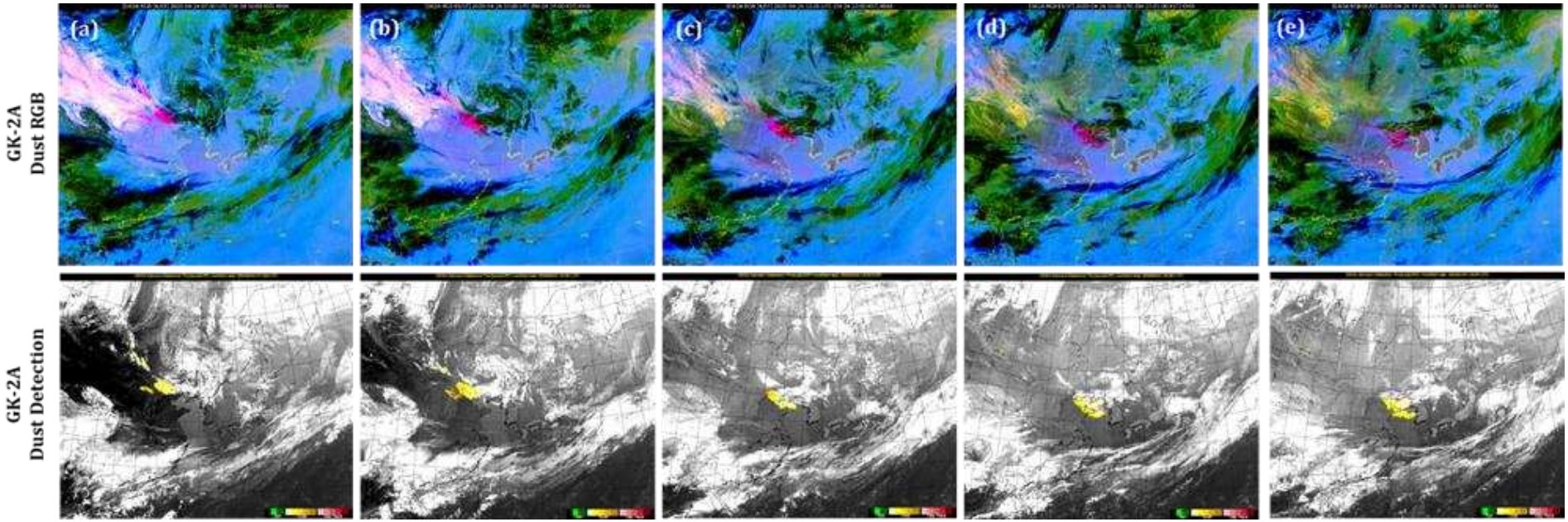

Figure 4. Example of the yellow dust detection using GK-2A's infrared channel threshold values at (a) 07:00 UTC; (b) 10:00 UTC; (c) 13:00 UTC; (d) 16:00 UTC; and (e) 19:00 (2020.05.24 03:00 UTC–11:00 UTC, intervals of 2 hours).

 doi:10.20944/preprints202312.1275.v1

3.1.2. Comparisons of dust imagery products during the daytime

For qualitative evaluation during the daytime, the dust RGB imagery was used, which was obtained through the same process described in Section 3.1.1. On May 11, 2020, at 03:00 UTC (12:00 KST), a dust storm originated in eastern Mongolia and extended to inner Mongolia, China (Figure 5). It was also observed on the Loess Plateau and west of the Shandong Peninsula at 00:00 UTC on May 12 (09:00 KST). According to the China Meteorological Administration (CMA), a high dust concentration of 800 $\boldsymbol{\mu g/m^3}$ or more was observed in inner Mongolia, such as in Erlenhot and Zhulihe, at 05:00 UTC on May 11, reaching a maximum of >3000 $\boldsymbol{\mu g/m^3}$. On May 12, the concentration in Dungseong, located on the Loess Plateau, began to rise, indicating that it was approaching the Korean Peninsula as it was biased to the southwest. Subsequently, dust storms were detected in the Yellow Sea and the central area of the Korean Peninsula through the Shandong Peninsula in China. In particular, the dust across the Korean Peninsula was strong. As a result of GK-2A aerosol detection product analysis, the image represented that dust was strongly penetrating the Korean Peninsula in a U-shape. From 03:00 UTC to 05:00 UTC on May 12 (Figure 5a,b), the concentration of dust generated strongly in southern China gradually weakened as it passed through the Yellow Sea, affecting the Korean Peninsula. Additionally, due to the improvement of the yellow dust detection algorithm, continuity between land and sea was well distinguished, enabling identification of the dust flow. From 07:00 UTC to 09:00 UTC (Figure 5c,d), dust that had affected the central region of the Korean Peninsula moved to the south and directly affected the southern coast at 11:00 UTC (Figure 5e). By using the GK-2A dust RGB, detection of dust movement became possible. The dark pink pixels in the dust RGB and the pixels in the GK-2A aerosol detection algorithm coincided, making it easy to accurately identify the location of yellow dust.

Preprints (www.preprints.org) | NOT PEER-REVIEWED | Posted: 18 December 2023 doi:10.20944/preprints202312.1275.v1

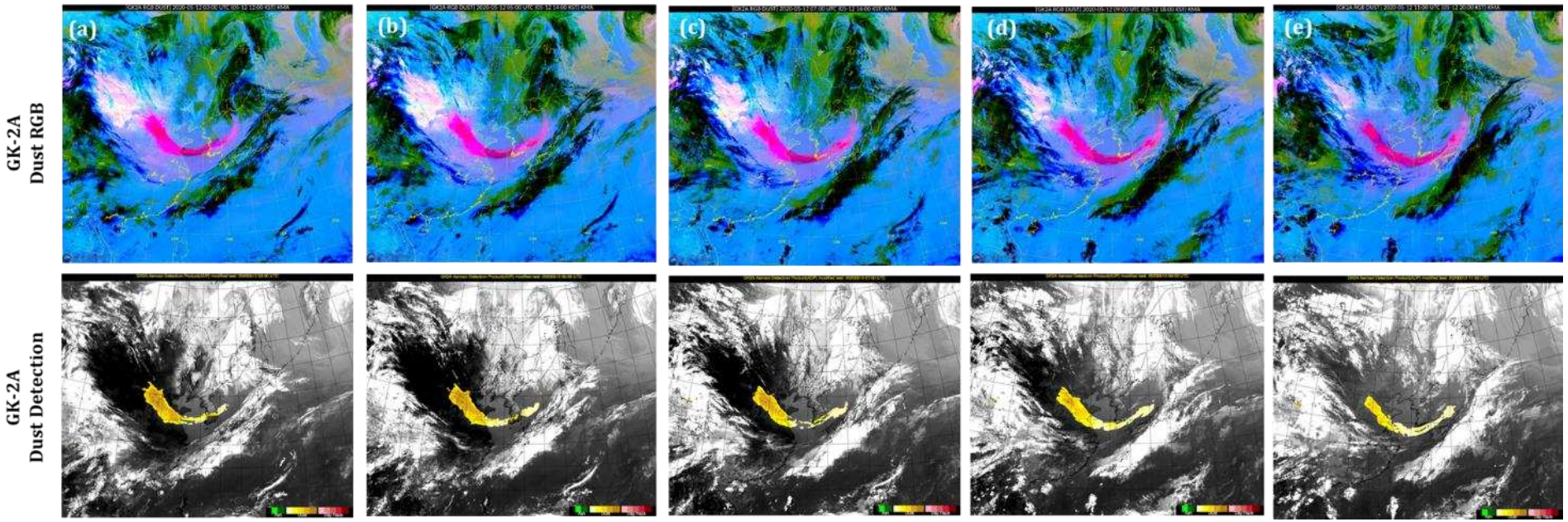

Figure 5. Example of the yellow dust detection using GK-2A's infrared channel threshold values at (a) 03:00 UTC; (b) 05:00 UTC; (c) 07:00 UTC; (d) 09:00 UTC; and (e) 11:00 UTC (2020.04.24 07:00 UTC–19:00 UTC, intervals of 3 hours).

 doi:10.20944/preprints202312.1275.v1

3.2. Correction of DAOD visible and infrared channels from GK-2A

3.2.1. GK-2A visible AOD spatial variability and retrieval accuracy

Under the assumption that the accuracy of the visible AOD of GK-2A must be secured to a certain extent, CDF fitting can be performed on the IR AOD. Therefore, confirming the accuracy of the visible AOD was essential. To confirm the accuracy of the visible AOD, AERONET was used, which provides ground observation data. The maps showing the location of the AERONET (Table 4) sun-sky radiometers utilized in this study are shown in Figure 6. AERONET data were used for cloud screening (Level 1.5) based on the dissimilar temporal frequencies between clouds and AOD. When the yellow dust occurred in East Asia in 2020, an AERONET point that matched the trajectory of the dust storm was selected, and only 40 sites could simultaneously utilize the data. The visible channel-based AOD and AERONET were compared for AERONET validation. Compared with AERONET AOD, GK-2A AOD values were close on the 1:1 line but showed a tendency to be underestimated in some pixels. Figure 6a shows the R, RMSE, and bias values of 0.83, 0.23, and 0.084, respectively. Additionally, as the aerosol loading increased (AOD > 1), the values got closer to the 1:1 line, indicating that the GK-2A AOD is superior in detecting high aerosol concentration plumes. However, there were pixels with AERONET AOD was above 1.5 (AERONET AOD > 1.5) but low value of GK-2A AOD because, before calculating the GK-2A AOD, the effect of aerosols was underestimated by over-detecting the surface reflectivity of the 30-day background composite field. Additionally, to confirm the accuracy of the GK2A visible AOD, the aerosol products were validated using the Suomi-NPP/VIIRS (Figure 6b) EDR AOD in northeast Asia. The inter-comparison of GK-2A visible AOD products and VIIRS AOD indicated that the GK-2A visible AOD products had an overall global bias of -0.0008 against VIIRS EDR AOD, whereas the corresponding values of the VIIRS IP AOD products were 0.0415 [13]. The validation of the GK-2A visible AOD demonstrated that the visible AOD retrievals exhibited good agreement with the VIIRS AOD observations (R = 0.651), and the GK-2A AOD products exhibited positive biases ($y = 0.61x + 0.038$) in a high aerosol loading area [52]. Similar to the AERONET results, when high-concentration aerosols were generated, the Suomi-NPP/VIIRS and GK-2A AOD were close to the 1:1 line, showing agreement. However, when the concentration of VIIRS was high, the disadvantage of under-detection of GK-2A appeared to be the same as that of AERONET; therefore, it needs improvement in the future.

Focusing on these 40 AERONET sites, Figure 6c,d and Table 5 summarize the regional variations in GK-2A visible AOD retrieval accuracy. The GK-2A visible AOD performed better in Korea and Japan than in Taiwan and China. In particular, the GK-2A AOD had a lower RMSE and bias at points closer to the Korean Peninsula, and more errors occurred farther away. Moreover, the Korean Peninsula branching Anmyon, Hankuk-UFS, Seoul-University, Yonsei-University, Gwangju Gist, Socheongcho, and Gangneung-WNU had RMSE as low as $0.07 - 0.13$, and the bias (AERONET − Observation) was underestimated at $0.0003 - 0.05$. However, in Japan, including FUKUE, Fukuoka, Shirahama, OSAKA, Chiba-University, Noto, Niigata, and Hokkaido, the RMSE was as low as 0.07−0.24, and the bias was overestimated at 0.006−0.067, except for Noto. Moreover, in China, including Xianghe, Beijing_CAMS, Beijing, and Beijing_radi showed an RMSE of 0.146−0.20 and bias of −0.023 to 0.01. It had an overestimation, similar to the Japanese region, but a low RMSE. In contrast, the Taiwan region, including Dongsha_island, Luang_namtha, mandaly_mtu, Bhola, Hong Kong _polyU, Hong Kong _sheung, Kaoshiung, Chenkung_University, Lulin, Douliu, Dhaka_University, Xitun, EPA_NCU, Taipei_CWB, Fuguei_ Cape, Dibrugarh_ University, and NAM_CO, showed a rather large RMSE and bias. Therefore, as a result of analyzing the accuracy of AERONET and GK-2A AOD by region, it tended to decrease as the distance increased from the Korean Peninsula. However, as this study focused on improving the accuracy of the IR and increasing the continuity of the DAOD during the day and night, it was conducted by considering the error of the AOD (assuming that the visible AOD is true).

Preprints (www.preprints.org) | NOT PEER-REVIEWED | Posted: 18 December 2023 doi:10.20944/preprints202312.1275.v1

Table 4. Details about the representative Aerosol Robotic Network (AERONET) site to validate for dust aerosol optical depth (DAOD).

Site	Latitude (Degree)	Longitude (Degree)	Elevation(m)	Type
Anmyon	36.539 N	126.330 E	47	Rural
AOE_Baotou	40.852 N	109.629 E	1,314	Rural
Beijing	39.977 N	116.381 E	92	Urban
Beijing-CAMS	39.933 N	116.317 E	106	Urban
Beijing-RADI	40.005 N	116.379 E	59	Urban
Bhola	22.227 N	90.756 E	7	
Chen-Kung_Univ	22.993 N	120.204 E	50	
Chiba_University	35.625 N	140.104 E	60	
Dalanzadgad	43.577 N	104.419 E	1,470	Rural
Dhaka_University	23.728 N	90.398 E	34	
Dibrugarh_Univ.	27.451 N	94.896 E	119	
Dongsha_island	20.699 N	116.729 E	5	
Douliu	23.712 N	120.545 E	60	
EPA-NCU	24.968 N	121.185 E	144	
Fuguei_Cape	25.297 N	121.538 E	50	
Fukue	32.752 N	128.682 E	80	
Fukuoka	33.524 N	130.475 E	30	
Gangneung_WNU	37.771 N	128.867 E	60	Suburban
Gwangju_GIST	35.228 N	126.843 E	52	Urban
Hankuk_UFS	37.339 N	127.266 E	167	
Hokkaido_University	43.075 N	141.341 E	59	
Hong_Kong_PolyU	22.393 N	114.180 E	30	
Hong_Kong_Sheung	22.483 N	114.117 E	40	
Irkutsk	51.800 N	103.087 E	670	
Kaohsiung	22.676 N	120.292 E	15	
Luang_Namtha	20.931 N	101.416 E	557	
Lulin	23.469 N	120.874 E	2868	
Mandalay_MTU	21.973 N	96.186 E	104	
NAM_CO	30.773 N	90.963 E	4746	
Niigata	37.846 N	138.942 E	10	
Noto	37.334 N	137.137 E	200	
Osaka	34.651 N	135.591 E	50	
Seoul_SNU	37.458 N	126.951 E	116	Urban
Shirahama	33.693 N	135.357 E	10	
Socheongcho	37.423 N	124.738 E	28	Ocean
Taipei_CWB	25.015 N	121.538 E	26	
Ussuriysk	43.700 N	132.163 E	280	
XiangHe	39.754 N	116.962 E	36	Urban
Xitun	24.162 N	120.617 E	91	
Yonsei_University	37.564 N	126.935 E	97	Uban

Table 5. Results of statistical error (RMSE, Bias) analysis about the representative Aerosol Robotic Network (AERONET) site to validate for GK-2A of Aerosol Optical Depth (AOD).

Site	Latitude/Longitude (Degree)	Colocation number	RMSE	Bias
Anmyon	36.539 N/126.330 E	1675	0.122	0.009
AOE_Baotou	40.852 N/109.629 E	1156	0.225	-0.111

 doi:10.20944/preprints202312.1275.v1

Beijing	39.977 N/116.381 E	1031	0.146	-0.023
Beijing-CAMS	39.933 N/116.317 E	1975	0.177	-0.017
Beijing-RADI	40.005 N/116.379 E	1871	0.191	-0.02
Bhola	22.227 N/90.756 E	1871	0.211	0.047
Chen-Kung_Univ	22.993 N/120.204 E	1404	0.273	0.062
Chiba_University	35.625 N/140.104 E	1165	0.13	-0.023
Dalanzadgad	43.577 N/104.419 E	2133	0.264	-0.155
Dhaka_University	23.728 N/90.398 E	681	0.224	0.078
Dibrugarh_Univ.	27.451 N/94.896 E	948	0.279	0.101
Dongsha_island	20.699 N/116.729 E	1526	0.176	0.052
Douliu	23.712 N/120.545 E	722	0.185	0.029
EPA-NCU	24.968 N/121.185 E	994	0.193	0.024
Fuguei_Cape	25.297 N/121.538 E	604	0.134	0.016
Fukue	32.752 N/128.682 E	1689	0.095	-0.006
Fukuoka	33.524 N/130.475 E	1767	0.141	-0.008
Gangneung_WNU	37.771 N/128.867 E	1343	0.13	0.032
Gwangju_GIST	35.228 N/126.843 E	565	0.134	0.003
Hankuk_UFS	37.339 N/127.266 E	1800	0.073	0.055
Hokkaido_University	43.075 N/141.341 E	918	0.237	-0.067
Hong_Kong_PolyU	22.393 N/114.180 E	591	0.18	-0.006
Hong_Kong_Sheung	22.483 N/114.117 E	860	0.13	0.006
Irkutsk	51.800 N/103.087 E	1105	0.101	-0.049
Kaohsiung	22.676 N/120.292 E	1626	0.24	0.062
Luang_Namtha	20.931 N/101.416 E	1745	0.496	0.222
Lulin	23.469 N/120.874 E	630	0.09	-0.013
Mandalay_MTU	21.973 N/96.186 E	2299	0.303	0.154
NAM_CO	30.773 N/90.963 E	639	0.261	-0.139
Niigata	37.846 N/138.942 E	1384	0.106	-0.014
Noto	37.334 N/137.137 E	1329	0.12	0.014
Osaka	34.651 N/135.591 E	1371	0.182	-0.023
Seoul_SNU	37.458 N/126.951 E	1655	0.137	0.034
Shirahama	33.693 N/135.357 E	516	0.028	-0.006
Socheongcho	37.423 N/124.738 E	1000	0.115	0.008
Taipei_CWB	25.015 N/121.538 E	761	0.248	0.126
Ussuriysk	43.700 N/132.163 E	870	0.094	0.012
XiangHe	39.754 N/116.962 E	1388	0.202	0.002
Xitun	24.162 N/120.617 E	1486	0.233	0.053
Yonsei_University	37.564 N/126.935 E	1436	0.136	0.049

Preprints (www.preprints.org) | NOT PEER-REVIEWED | Posted: 18 December 2023 doi:10.20944/preprints202312.1275.v1

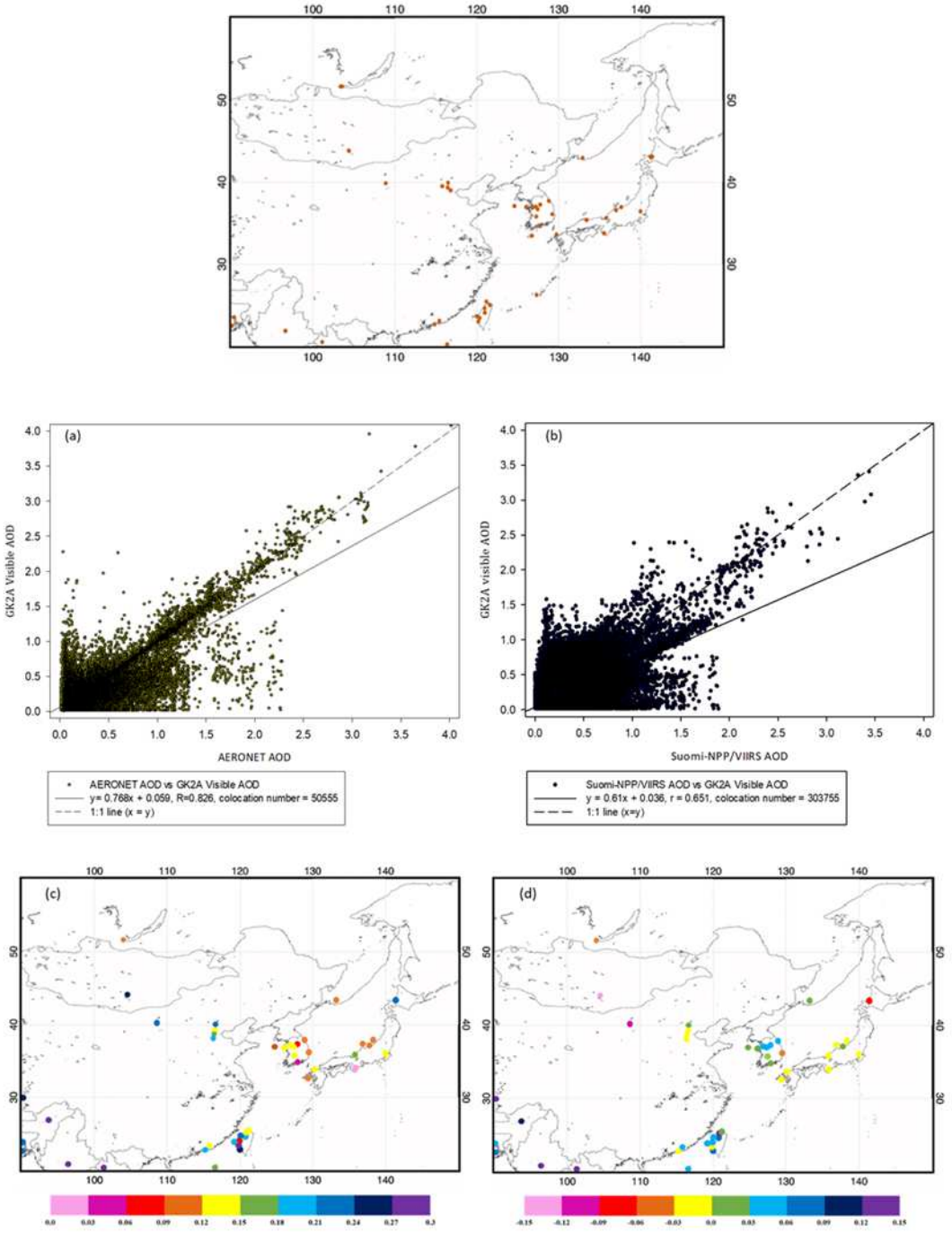

Figure 6. Locations of the 40 selected Aerosol Robotic Network (AERONET) sites used for comparisons of aerosol optical depth (AOD). Validation results of GK-2A AOD, AERONET(a), and Suomi-NPP/VIIRS(b) AOD in the 2020 yellow dust case. Results of statistical error (RMSE (c), Bias (d)) analysis of GK-2A AOD and AERONET AOD.

3.2.2. Bias correction of GK-2A infrared DAOD

To maintain continuity in the visible and IR channels of the DAOD, CDFs were applied to the dust events in 2020. To validate the accuracy of DAOD, a representative case of yellow dust was tested using 2021 data. The goal was to maximize the accuracy of the DAOD value while tracking the accuracy of the visible-channel DAOD. This method assumes that the visible DAOD is true and applies a method for fitting the IR DAOD. This is because the visible DAOD is calculated based on

Preprints (www.preprints.org) | NOT PEER-REVIEWED | Posted: 18 December 2023 doi:10.20944/preprints202312.1275.v1

reflectivity and the IR DAOD is calculated based on radiation, and their purposes of calculation are different, and each Lookup Table (LUT) is different, limiting consistency. However, the statistical CDF fitting method was adopted by focusing on the technology to correct errors faster and more quickly. CDFs were applied to individual grid cells to increase the accuracy of the IR DAOD based on the visible DAOD. The CDFs of DAOD during the training data (dust event in 2020) are shown in Figure 7. Notably, the DAOD of the visible was evenly distributed within the range of 0−4, while the DAOD of the IR was cumulated in the range of 0.5−1.6. In addition, at the starting point of the AOD of 1.6, the visible and IR AOD crossed, and the fitting curve was reversed. In other words, it does not detect low dust concentration of 0−0.5 μm, and tends to underdetect strong yellow dust. Since the DAOD of GK-2A was calculated only for yellow dust pixels, the sensitivity of DAOD using the IR channel was greater, and the concentration of DAOD tended to be high. In fact, because the DAOD of yellow dust was observed at a high concentration rather than at a low concentration of 0.5, it is estimated that this is the result of reflection. Therefore, in this study, the tendency of the fitting curve was different based on a DAOD of 1.6; therefore, the coefficient was applied by bisecting it. The regression coefficients for each dust pixel were calculated, and Figure 8 shows the piecewise linear CDF fitting across the GK-2A satellite imagers analyzed for 2020. From the CDF fitting curve, the DAOD of the IR was overestimated rather than the DAOD of the visible within the range of 0 to 1.6 of DAOD (Figure 8a), and the IR of DAOD was underestimated than the visible DAOD within the range of 1.6−4.0 of DAOD (Figure 8b). Therefore, the coefficients were derived by dividing each concentration range of DAOD. Even though each range was set and applied, the frequency of the data was small in the range of DAOD 1.6 to 4.0, and the duration of high concentration was short, indicating an even distribution of data.

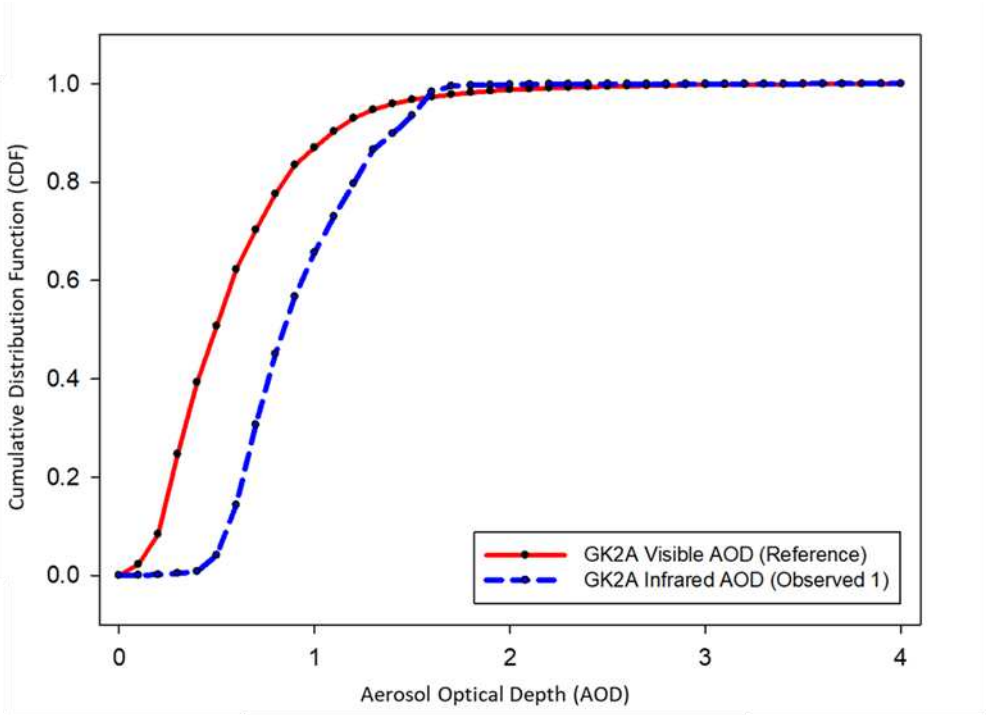

Figure 7. Cumulative distribution function (CDF) analysis results of Visible and Infrared aerosol optical depth (AOD) focusing on the 2020 yellow dust episodes.

Preprints (www.preprints.org) | NOT PEER-REVIEWED | Posted: 18 December 2023 doi:10.20944/preprints202312.1275.v1

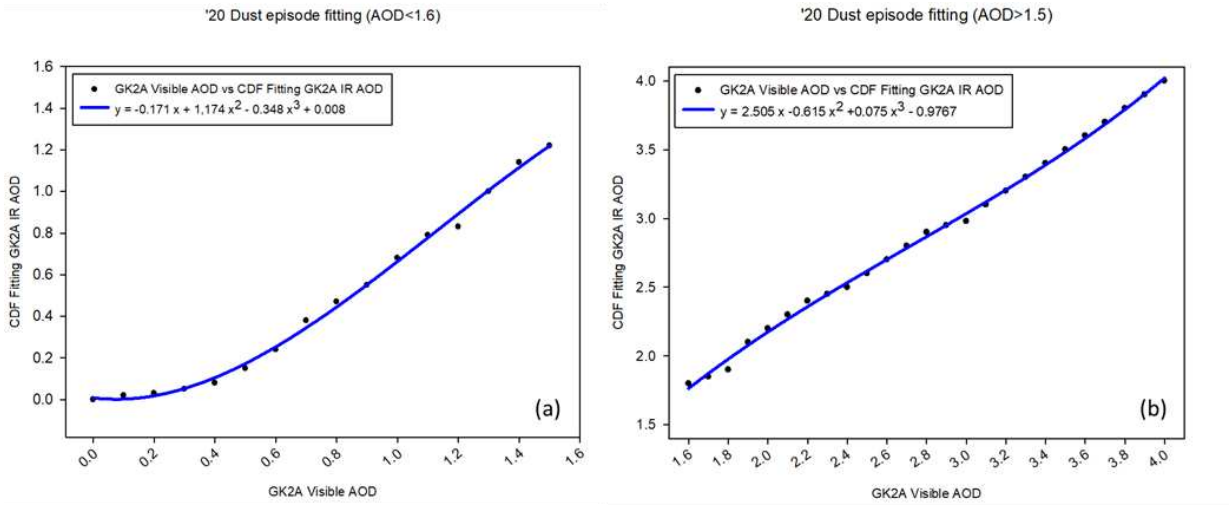

Figure 8. Cumulative distribution function (CDF) fitting analysis results of aerosol optical depth (AOD) <1.6 (a) and AOD >1.5 (b) focusing on the 2020 yellow dust episodes.

3.2.3. Accuracy of infrared DAOD applied to coefficient (correction factor)

To validate accuracy, it was conducted using the IR DAOD product of GK-2A. In previous studies, the coefficients calculated using the CDF fitting method have been applied to the GK-2A DAOD. The data used in this study were only the dust detection pixels for the period of the 2021 dust episodes. Figure 9 shows the scatterplots of AERONET versus GK-2A IR DAOD before (Figure 9a) and after (Figure 9b) bias correction for dust pixels. First, the DAOD before correction based on pixels co-located with AERONET showed very low accuracy based on the x = y (1:1) line. The original AMI DAOD had a correlation coefficient of 0.352, slope of 0.314, and offset of 0.417. AERONET was developed based on 500 nm (visible) and DAOD was developed based on 1050 nm (IR); therefore, differences inevitably occurred. This study aimed to develop a nighttime DAOD and ensure continuous monitoring alongside daytime DAOD, which was a challenging task. However, the visible channel AOD and DAOD after CDF fitting showed improved results and a trend similar to the 1:1 line (after bias correction, the correlation improved to 0.691, while the slope and offsets improved to 0.806 and 0.134, respectively). It was estimated to be improved as the value of DAOD shows that over-detection is relieved when AERONET's AOD (0.5–1.0) is small, and a similar tendency is shown when AERONET's AOD shows a high concentration.

Figure 10 shows a histogram of the original (uncorrected, Figure 10a) and CDF fitting (corrected, Figure 10b) IR DAOD pixels over the dust detection pixels (the same observation time as the DAOD data shown in Figure 9). The standard of visible AOD had a high frequency in the range of 0.3, which gradually decreased with increasing concentration. Although the IR DAOD before bias correction had many frequencies in the range of 0.7, it showed a tendency to not detect well at concentrations lower than 0.5 and higher than 1.6. This estimated DAOD is only with the pixels detected as dust, which means that when dust occurs, the concentration is high, and a small concentration of less than 0.5 cannot be detected even in the IR channel [53]. As a result of the analysis after applying the CDF method, the number showing high frequency at DAOD 0.7 was moved to the left, and the frequency showing low concentration increased. Therefore, the visible and IR DAOD were consistent, and their concentration distribution showed a similar tendency.

Preprints (www.preprints.org) | NOT PEER-REVIEWED | Posted: 18 December 2023 doi:10.20944/preprints202312.1275.v1

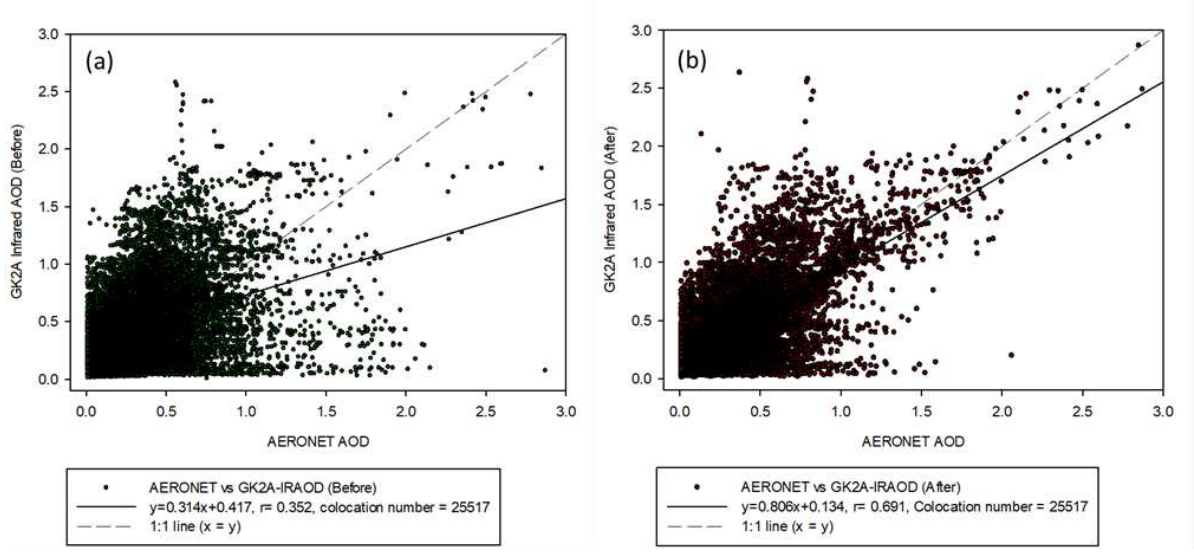

Figure 9. Validation results of GK-2A Infrared aerosol optical depth (AOD) before (a) and after (b) applying cumulative distribution function (CDF) fitting method.

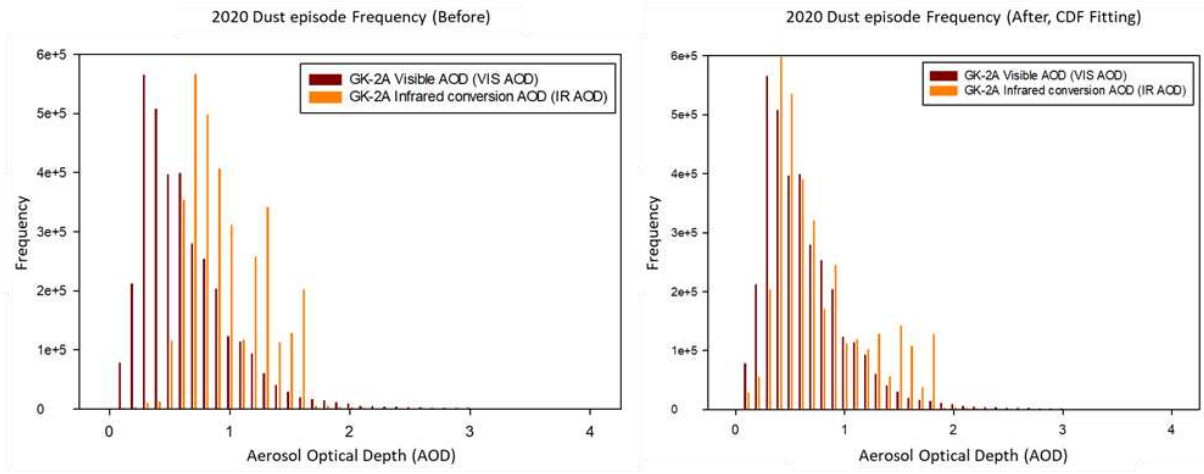

Figure 10. Histogram frequency results of GK-2A Infrared aerosol optical depth (AOD) before (a) and after (b) applying cumulative distribution function (CDF) fitting method.

3.3. Qualitative comparisons through intense dust events

Asian dust originates in the deserts of the Taklamakan, Mongolia, northern China and Kazakhstan and travels to China, North and South Korea, and Japan, where it particularly impacts human health and air quality. [54,55]. It is a well-known phenomenon that occurs during springtime in northeast Asia and also occurs frequently in fall and winter. After applying the coefficients derived from the 2020 training dataset, the GK-2A DAOD was computed and applied for dust events that occurred in 2021.

3.3.1. Spring dust transport over the Korean Peninsula on March 23−28, 2021

On March 21, 2021, yellow dust originated from the Gobi Desert and the inner Mongolian highlands. This dust came down with a northwest wind on March 23, which was detected in northern and northeastern China and on the Korean Peninsula. At that time, the concentration of PM_{10} at 04:00 UTC was observed in Sokcho to be 262 $\mu g/m^3$, Daegwallyeong to be 247 $\mu g/m^3$, Mungyeong to be 206 $\mu g/m^3$, and Uljin to be 162 $\mu g/m^3$. The yellow dust that occurred on March 21 gradually faded, but again on March 26 at 04:00 UTC, yellow dust was observed in the inner Mongolian plateau, and the concentration of PM_{10} in Zuricher was 838 $\mu g/m^3$ and Erlenhot was 1,226 $\mu g/m^3$. After that,

 doi:10.20944/preprints202312.1275.v1

PM_{10} was observed in some areas of the Korean peninsula at 09:00 UTC; however it was slightly affecting at 141 $\mu g/m^3$ in Seoul, 132 $\mu g/m^3$ in Suwon, 105 $\mu g/m^3$ in Ganghwa, 100 $\mu g/m^3$ in Gwanaksan, and 100 $\mu g/m^3$ in Gwangju. Figure 11 shows the dust detection, visible DAOD, and IR DAOD obtained by GK-2A on March 26−28 from 23:00 UTC to 01:00 UTC at 5 h intervals based on the use of the developed algorithm. Based on the improved results, continuity and detection speed were increased by detecting regardless of the characteristics of the ground surface. Therefore, the area for detecting the DAOD at night increased, and the flow of yellow sand observed in Mongolia along the northwest wind could be effectively monitored. Over time, the yellow dust approached the Korean Peninsula, and when it originated, the DAOD of both the visible and IR channels was at high concentrations of 0.8 or higher (Figure 11a). After 5 h, the concentration began to decrease and fell to 0.4 (Figure 11b,c). Additionally, while the DAOD of the visible region was observed at various concentration ranges, the DAOD of the IR region exhibited a concentration of 0.4–0.8. After the twilight period, only the DAOD of IR could be observed at nighttime (Figure 11d,e), confirming that the DAOD was observed at the same location as the dust detection, and clouds and dust were mixed while approaching the Korean Peninsula at 19:00 UTC. After 5 h (Figure 11f), both visible and IR were observed during the daytime after dawn, and the concentration increased; however, the visible DAOD showed a higher concentration than the IR DAOD.

Preprints (www.preprints.org) | NOT PEER-REVIEWED | Posted: 18 December 2023 doi:10.20944/preprints202312.1275.v1

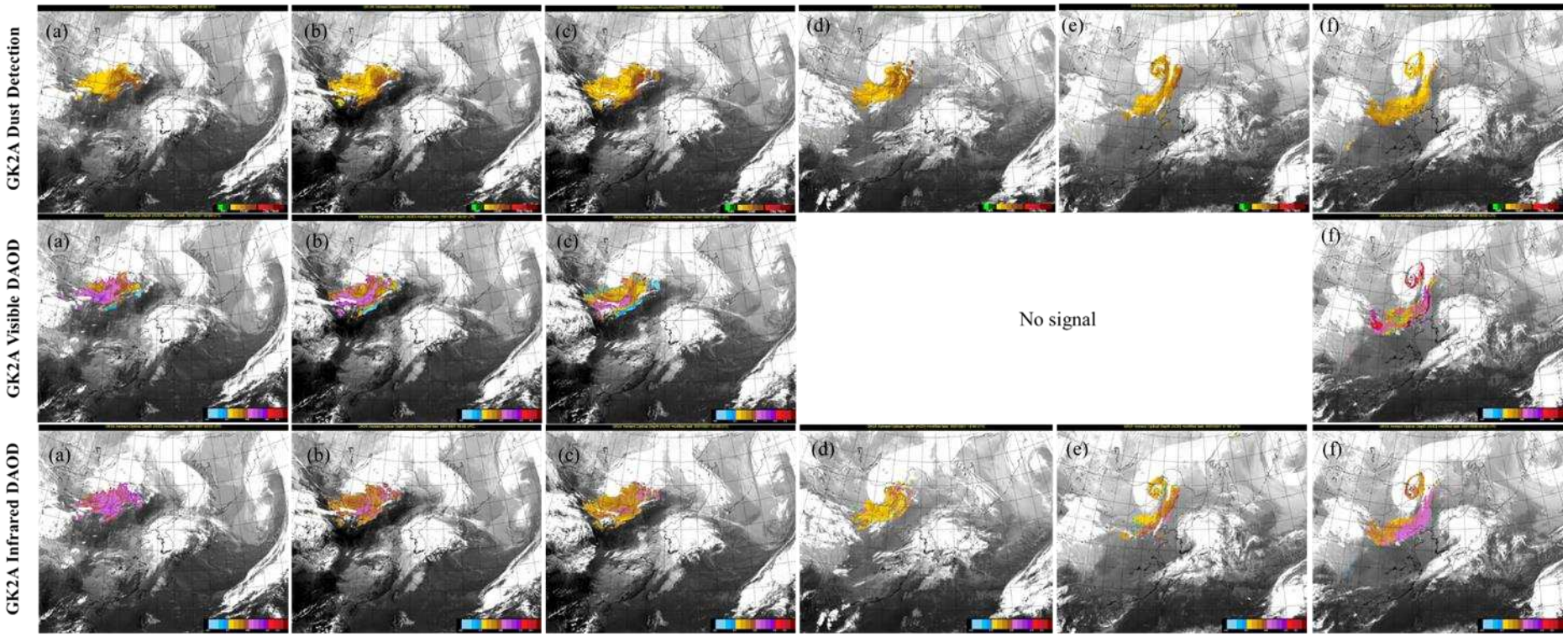

Figure 11. Images of Asian dust based on GK-2A Dust detection, GK-2A Visible Dust Aerosol Optical Depth (DAOD), GK-2A Infrared DAOD on March 26–28, 2021 (a) 26, 23:00 UTC; (b) 27, 04:00 UTC; (c) 27, 09:00 UTC; (d) 27, 14:00 UTC; € 27, 19:00 UTC; and (f) 28, 01:00 UTC.

 doi:10.20944/preprints202312.1275.v1

3.3.2. Example of dust transport over the Korean Peninsula on April 14−16, 2021 (spring dust)

On April 14, yellow dust originating from the Gobi Desert affected Bohai Bay. At 04:00 UTC on April 15, dust was detected by satellites in areas such as the Gobi Desert in southern Mongolia, northern China, and the Inner Mongolian Highlands. The concentrations of PM_{10} were 3342 $\mu g/m^3$ at Zurcher, 1552 $\mu g/m^3$ at Erlenhot, and 886 $\mu g/m^3$ at Dongseong, which were affected by the high concentration of dust. Figure 12 shows the dust detection, visible DAOD, and IR DAOD obtained by GK-2A on April 14−16 from 23:00 UTC to 01:00 UTC at 5 h intervals based on the use of the developed algorithm. A northeast-southwest directional V-shaped band passing through the West Sea first flowed in and affected the Korean Peninsula; as time passed, yellow dust was introduced again. When it first entered, a high concentration of 1.0 or higher (Figure 12a–c) was observed approaching in the form of cloud penetration. Yellow sand mixed with clouds was detected, and its concentration decreased over time. At night (Figure 12d,e), dust was observed at the same location, and the concentration ranged from 0.4 to 1.0, and the DAOD became thicker in the form of penetrating into the cloud. After dawn, the dust increased again during the day (Figure 12f), and both visible and IR DOAD appeared to be at the same concentration.

Preprints (www.preprints.org) | NOT PEER-REVIEWED | Posted: 18 December 2023 doi:10.20944/preprints202312.1275.v1

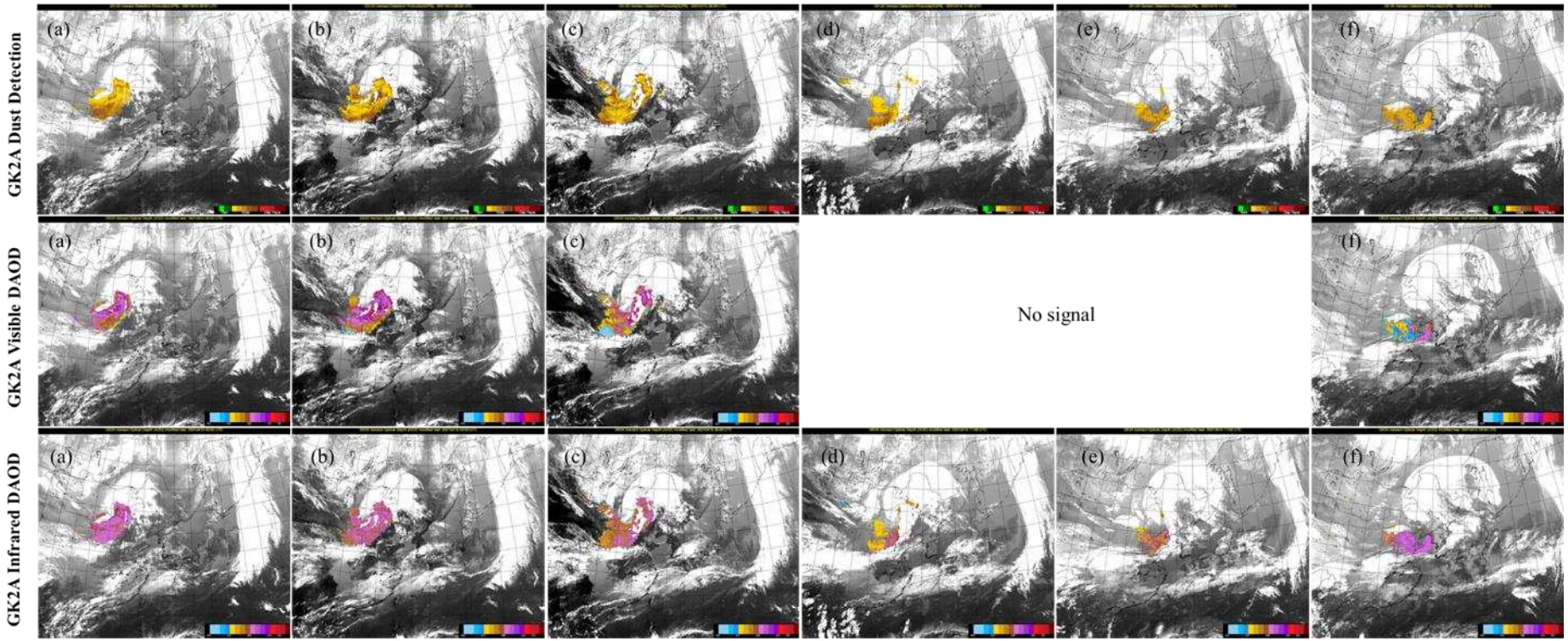

Figure 12. Images of Asian dust based on GK-2A Dust detection, GK-2A Visible Dust Aerosol Optical Depth (DAOD), GK-2A Infrared DAOD on April 14–16, 2021. (a) 14, 23:00 UTC; (b) 15, 04:00 UTC; (c) 15, 09:00 UTC; (d) 15, 14:00 UTC; (e) 15, 19:00 UTC; and (f) 16, 01:00 UTC.

 doi:10.20944/preprints202312.1275.v1

3.3.3. Example of dust transport over the Korean Peninsula on May 4−8, 2021 (spring dust)

The event of May 5−8, 2021, was selected for being the longest-lasting yellow dust event in 2021. On May 3, the dust storm originated from the Gobi, Northern China, and Inner Mongolian Highlands and continued to affect the region until May 7. Figure 13 shows the dust detection, visible DAOD, and IR DAOD obtained by GK-2A on May 5−7 from 23:00 UTC to 01:00 UTC at 5 h intervals based on the use of the developed algorithm. The yellow dust piled up with clouds and approached the Korean Peninsula in a circle resembling a pig's tail. When it originated in a form similar to the previous two cases, it showed a tendency to approach with a thick concentration and then fade, and it appeared that yellow dust penetrated between the cloud belt located under the Korean Peninsula and clouds located in China (Figure 13a–c) during the daytime. In particular, the DAOD values of 0.4 to 0.9 at night (Figure 13d,e), were effective in monitoring the movement of dust. Consequently, during the daytime after 5 h (Figure 13f), the concentration of dust moving between clouds tended to be consistent with the concentration of 1.0; however, in the flow of dust that followed, it appeared somewhat higher in the IR channel.

Preprints (www.preprints.org) | NOT PEER-REVIEWED | Posted: 18 December 2023 doi:10.20944/preprints202312.1275.v1

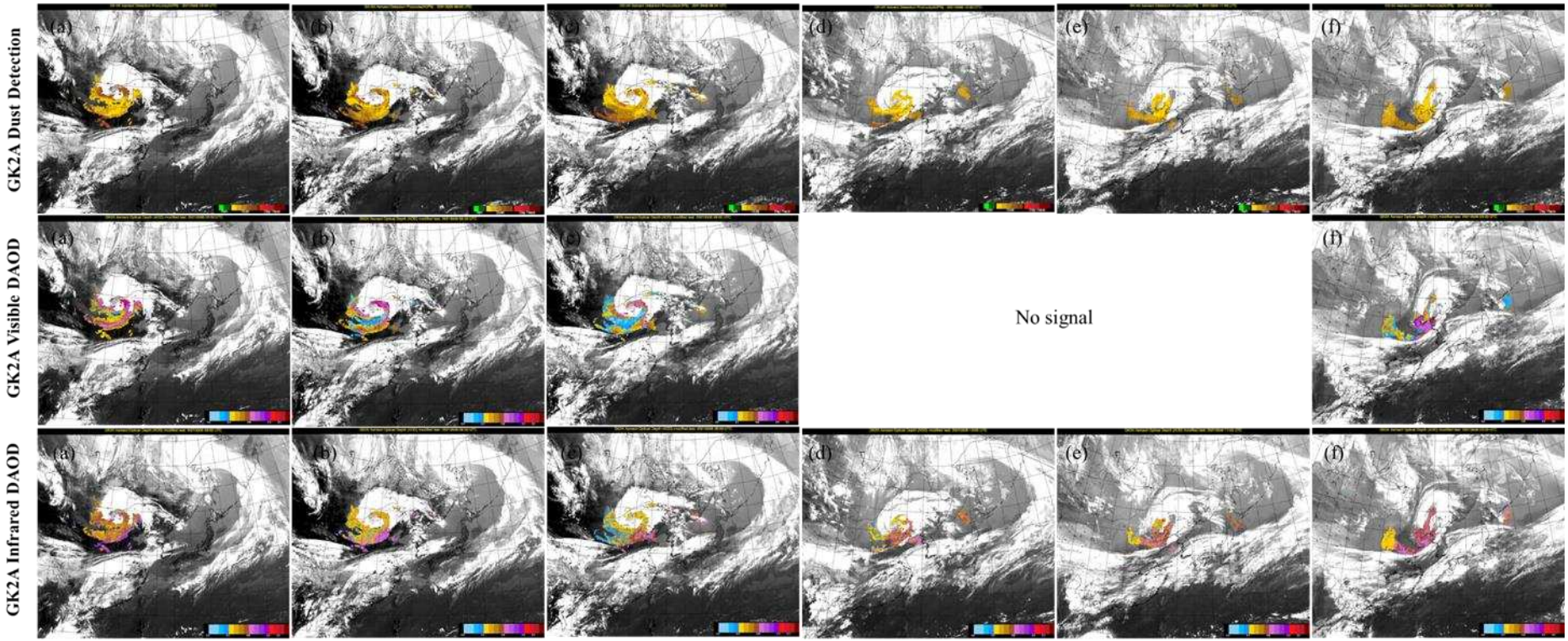

Figure 13. Images of Asian dust based on GK-2A Dust detection, GK-2A Visible Dust Aerosol Optical Depth (DAOD), GK-2A Infrared DAOD on May 5–7, 2021 (a) 5, 23:00 UTC; (b) 6, 04:00 UTC; (c) 6, 09:00 UTC; (d) 6, 14:00 UTC; (e) 6, 19:00 UTC; and (f) 7, 01:00 UTC.

Preprints (www.preprints.org) | NOT PEER-REVIEWED | Posted: 18 December 2023 doi:10.20944/preprints202312.1275.v1

3.4. Quantitative comparison between GK-2A DAOD and Calipso/Caliop over the period of dust events in 2021 (validation)

For the quantitative validation of the GK-2A DAOD, CALIPSO was used, which has a vertical profile in northeast Asia for 2021. The reason for using the CALIPSO satellite for quantitative analysis was that most of the DAOD was calculated only during the daytime, and it can be used to validate the DAOD calculated at night developed in this study. The CALIPSO satellite is a passive satellite that cannot detect large areas owing to its narrow swath; However, it was the only data to validate DAOD at night, and it is valuable data that can only be verified after passing that time and point. [56]. Since the CALIPSO satellite observes the Korean Peninsula once during the day and night, the time when the dust occurred and the time when the CALIPSO passed should be the same; therefore, there were limitations in the validation case. To validate the data, the CALIPSO/CALIOP AOD at 10.2 μm was used for retrieval during the 10 min observation period of the GK-2A IR DAOD. By selecting point within a 10 km radius of the CALIPSO pixel, the GK-2A DAOD grid was determined to be the nearest point. In this study, it was validated when the CALIPSO data and GK-2A matched the approach of yellow dust over the Korean Peninsula at nighttime at 19:10 UTC on April 15, 2021 (CAL_LID_L2_VFM_ValStage1-V3-41.2021-04-15T-10-53ZN. hdf). Yellow dust was strongly detected in the GK-2A dust detection retrieval (Figure 14a), and GK-2A AOD (Figure 14b) was also observed at a high concentration in the range of 0.7–1.3. Especially from CALIPSO observed at night, the yellow sand was found to be floating high at latitude 38° at the same location as GK-2A at approximately 8.5 to 9 km from CALIPSO 10.2 nm AOD, and the value was measured up to 1.3. In contrast, the low-lying yellow dust was estimated to be approximately 4 km, and the GK-2A DAOD and colocation pixels were the same at 0.7. When dust occurs at night, validation is difficult because the two satellites must match at the same time. However, meaningful results can be obtained by inferring the quantitative values of dust, particularly at night, using the validation case.

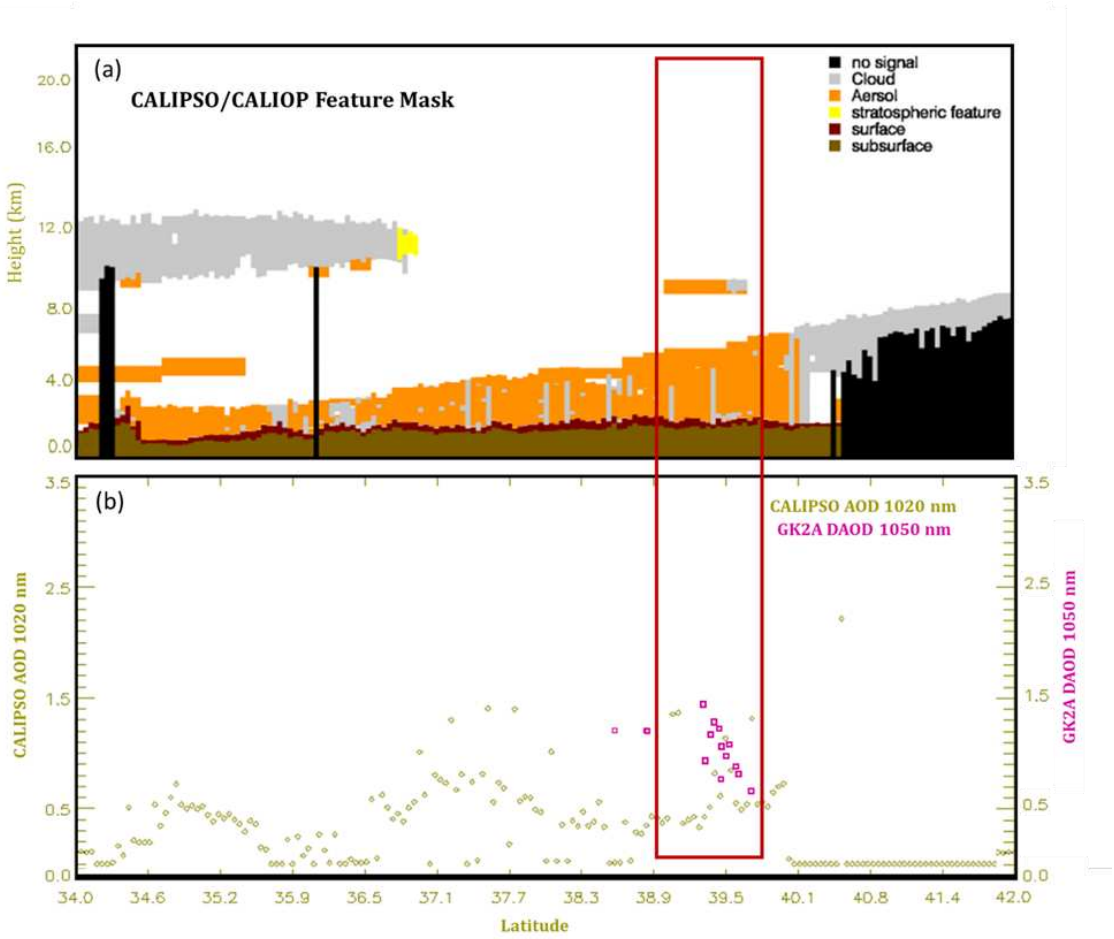

 doi:10.20944/preprints202312.1275.v1

Figure 14. Validation results after matching CALIOP/CALIPSO Infrared aerosol optical depth (AOD) (1020 nm) and GK-2A Infrared AOD (1050 nm).

4. Summary and Conclusions

Based on the developed and improved IR DAOD of GK-2A, multispectral data can be obtained for dust plumes. In particular, based on the analysis of observation data, we developed a dust storm mask algorithm to pinpoint dust detection and direction, flow. The dust detection algorithm is based on the multi-threshold IR (8.7, 10.5, 11.2, and 12.3 μm) BTD-BBTD ratio. This algorithm can be used under 24-hour conditions for the identification of yellow dust. In this study, the performance of the GK-2A visible AOD in north-east Asia was evaluated against AERONET and Suomi-NPP/VIIRS. The first part of the IR DAOD was presented utilizing a CDF fitting method to retrieve the column properties of atmospheric aerosols from the GK-2A visible AOD. The accuracy of GK-2A IR DAOD data was assessed using collocated measurements with ground observations, and spatial-temporal variability was examined using CALIPSO/CALIOP.

The main conclusions of this study are as follows:

1. The GK-2A/AMI DAOD was developed for detecting yellow sand in northeast Asia, especially for continuous monitoring during the day and night.
2. The GK-2A/AMI AOD had an overall high correlation with AERONET (R = 0.691) and Suomi-NPP/VIIRS (R = 0.651).
3. The developed DAOD had a difference in the accuracy of the visible AOD; thus, its accuracy was improved by using a CDF fitting method, assuming that the visible AOD is true.
4. After the DAOD correction, it was validated with AERONET quantitatively and qualitatively to improve the results. In particular, when yellow dust appeared, the movement flow of the dust was monitored and showed continuity for 24 h.
5. Validation of the DAOD with CALIPSO/CALIOP at night showed quantitative values similar to 1020 nm for the CALIPO product, enabling the persistence of the height and attribute of the dust at the time of occurrence.

This study was performed to calculate the DAOD even at night using the characteristics of the IR channel and to use it for forecasting more accurate values. However, only pixels detected as dust were used because yellow dust occurred, and among those pixels, there were few cases in which the time and space coincided with polar orbiting satellites; above all, verification was limited. In the future, more cases of dust will be used to perform qualitative and quantitative validations, and problems such as under-detection will be improved.

Author Contributions: S.A. conceived and designed the experiments; S.A. performed the experiments; S.A. and H.-S.K. analyzed the data; S.A. and H.-S.K. and H.-C.L. contributed reagents/materials/analysis tools; S.A. wrote the paper; J.-Y.B. managed the entire research process. All authors have read and agreed to the published version of the manuscript

Funding: This study received no external funding.

Institutional Review Board Statement: Not applicable.

Informed Consent Statement: Not applicable.

Data Availability Statement: Informed Consent Statement: Data are available on request owing to restrictions such as privacy or ethics. Data presented in this study are available upon request from the corresponding author.

Acknowledgments: This research was supported by the "Technical Development on Weather Forecast Support and Convergence Service using Meteorological Satellites" of the NMSC/KMA (Grant No. KMA2020-00121).

Conflicts of Interest: The authors declare no conflicts of interest.

References

1. Che, H. Z., Shi, G. Y., Zhang, X. Y., Zhao, J. Q., & Li, Y. (2007). Analysis of sky conditions using 40 year records of solar radiation data in China. *Theoretical and Applied Climatology*, *89*(1), 83-94.

2. Cheng, S. H., Yang, L. X., Zhou, X. H., Xue, L. K., Gao, X. M., Zhou, Y., & Wang, W. X. (2011). Size-fractionated water-soluble ions, situ pH and water content in aerosol on hazy days and the influences on visibility impairment in Jinan, China. *Atmospheric Environment*, *45*(27), 4631-4640.
3. Liang, F., & Xia, X. A. (2005, October). Long-term trends in solar radiation and the associated climatic factors over China for 1961-2000. In *Annales Geophysicae* (Vol. 23, No. 7, pp. 2425-2432). Copernicus GmbH.
4. Menon, S., Hansen, J., Nazarenko, L., & Luo, Y. (2002). Climate effects of black carbon aerosols in China and India. *Science*, *297*(5590), 2250-2253.
5. Xu, J., Bergin, M. H., Yu, X., Liu, G., Zhao, J., Carrico, C. M., & Baumann, K. (2002). Measurement of aerosol chemical, physical and radiative properties in the Yangtze Delta region of China. *Atmospheric Environment*, *36*(2), 161-173.
6. Pope, C. A., Dockery, D. W., & Schwartz, J. (1995). Review of epidemiological evidence of health effects of particulate air pollution. *Inhalation Toxicology*, *7*(1), 1-18.
7. Yu, F., Luo, G., & Ma, X. (2012). Regional and global modeling of aerosol optical properties with a size, composition, and mixing state resolved particle microphysics model. *Atmospheric Chemistry and Physics*, *12*(13), 5719-5736.
8. Hauser, A., Oesch, D., Foppa, N., & Wunderle, S. (2005). NOAA AVHRR derived aerosol optical depth over land. *Journal of Geophysical Research: Atmospheres*, *110*(D8).
9. Hauser, A., Oesch, D., & Foppa, N. (2005). Aerosol optical depth over land: Comparing AERONET, AVHRR and MODIS. *Geophysical Research Letters*, *32*(17).
10. Torres, O., Tanskanen, A., Veihelmann, B., Ahn, C., Braak, R., Bhartia, P. K., ... & Levelt, P. (2007). Aerosols and surface UV products from Ozone Monitoring Instrument observations: An overview. *Journal of Geophysical Research: Atmospheres*, *112*(D24).
11. Kahn, R. A., Gaitley, B. J., Garay, M. J., Diner, D. J., Eck, T. F., Smirnov, A., & Holben, B. N. (2010). Multiangle Imaging SpectroRadiometer global aerosol product assessment by comparison with the Aerosol Robotic Network. *Journal of Geophysical Research: Atmospheres*, *115*(D23).
12. Remer, L. A., Mattoo, S., Levy, R. C., & Munchak, L. A. (2013). MODIS 3 km aerosol product: algorithm and global perspective. *Atmospheric Measurement Techniques*, *6*(7), 1829-1844.
13. Huang, J., Kondragunta, S., Laszlo, I., Liu, H., Remer, L. A., Zhang, H., ... & Petrenko, M. (2016). Validation and expected error estimation of Suomi-NPP VIIRS aerosol optical thickness and Ångström exponent with AERONET. *Journal of Geophysical Research: Atmospheres*, *121*(12), 7139-7160.
14. Liu, H., Remer, L. A., Huang, J., Huang, H. C., Kondragunta, S., Laszlo, I., ... & Jackson, J. M. (2014). Preliminary evaluation of S-NPP VIIRS aerosol optical thickness. *Journal of Geophysical Research: Atmospheres*, *119*(7), 3942-3962.
15. Nakajima, T., Nakajima, T. Y., Higurashi, A., Sano, I., Takamura, T., Ishida, H., & Schutgens, N. (2008). A study of aerosol and cloud information retrievals from CAI imager on board GOSAT satellite. *Journal of the Remote Sensing Society of Japan*, *28*(2), 178-189.
16. Capelle, V., Chédin, A., Siméon, M., Tsamalis, C., Pierangelo, C., Pondrom, M., ... & Scott, N. A. (2014). Evaluation of IASI-derived dust aerosol characteristics over the tropical belt. *Atmospheric Chemistry and Physics*, *14*(17), 9343-9362.
17. Cuesta, J., Eremenko, M., Flamant, C., Dufour, G., Laurent, B., Bergametti, G., ... & Zhou, D. (2015). Three-dimensional distribution of a major desert dust outbreak over East Asia in March 2008 derived from IASI satellite observations. *Journal of Geophysical Research: Atmospheres*, *120*(14), 7099-7127.
18. Vogelmann, A. M., Flatau, P. J., Szczodrak, M., Markowicz, K. M., & Minnett, P. J. (2003). Observations of large aerosol infrared forcing at the surface. *Geophysical Research Letters*, *30*(12).
19. Ginoux, P. (2017). Warming or cooling dust?, *Nature Geoscience*, *10*(4), 246-248.
20. Heinold, B., Knippertz, P., Marsham, J. H., Fiedler, S., Dixon, N. S., Schepanski, K., ... & Tegen, I. (2013). The role of deep convection and nocturnal low-level jets for dust emission in summertime West Africa: Estimates from convection-permitting simulations. *Journal of Geophysical Research: Atmospheres*, *118*(10), 4385-4400.
21. Hourdin, F., Gueye, M., Diallo, B., Dufresne, J. L., Escribano, J., Menut, L., ... & Guichard, F. (2015). Parameterization of convective transport in the boundary layer and its impact on the representation of the diurnal cycle of wind and dust emissions. *Atmospheric Chemistry and Physics*, *15*(12), 6775-6788.
22. Kocha, C., Tulet, P., Lafore, J. P., & Flamant, C. (2013). The importance of the diurnal cycle of Aerosol Optical Depth in West Africa. *Geophysical Research Letters*, *40*(4), 785-790.

23. Heinold, B., Knippertz, P., Marsham, J. H., Fiedler, S., Dixon, N. S., Schepanski, K., ... & Tegen, I. (2013). The role of deep convection and nocturnal low-level jets for dust emission in summertime West Africa: Estimates from convection-permitting simulations. *Journal of Geophysical Research: Atmospheres*, *118*(10), 4385-4400.
24. Holben, B. N., Eck, T. F., Slutsker, I. A., Tanre, D., Buis, J. P., Setzer, A., ... & Smirnov, A. (1998). AERONET—A federated instrument network and data archive for aerosol characterization. *Remote sensing of environment*, *66*(1), 1-16.
25. Jackson, J. M., Liu, H., Laszlo, I., Kondragunta, S., Remer, L. A., Huang, J., & Huang, H. C. (2013). Suomi-NPP VIIRS aerosol algorithms and data products. *Journal of Geophysical Research: Atmospheres*, *118*(22), 12-673.
26. Omar, A. H., Winker, D. M., Vaughan, M. A., Hu, Y., Trepte, C. R., Ferrare, R. A., ... & Liu, Z. (2009). The CALIPSO automated aerosol classification and lidar ratio selection algorithm. *Journal of Atmospheric and Oceanic Technology*, *26*(10), 1994-2014.
27. Young, S. A., & Vaughan, M. A. (2009). The retrieval of profiles of particulate extinction from Cloud-Aerosol Lidar Infrared Pathfinder Satellite Observations (CALIPSO) data: Algorithm description. *Journal of Atmospheric and Oceanic Technology*, *26*(6), 1105-1119.
28. Jee, J. B., Lee, K. T., Lee, K. H., & Zo, I. S. (2020). Development of GK-2A AMI aerosol detection algorithm in the East-Asia region using Himawari-8 AHI data. *Asia-Pacific Journal of Atmospheric Sciences*, *56*(2), 207-223.
29. Ahn, S., Jee, J. B., Lee, K. T., & Oh, H. J. (2021). Enhanced accuracy of airborne volcanic ash detection using the GEOKOMPSAT-2A Satellite. *Sensors*, *21*(4), 1359.
30. Liu, Y., & Key, J. R. (2002, June). Detection and analysis of low-level temperature inversions with MODIS. In *IEEE International Geoscience and Remote Sensing Symposium* (Vol. 4, pp. 2308-2310). IEEE.
31. Ackerman, S. A. (1997). Remote sensing aerosols using satellite infrared observations. *Journal of Geophysical Research: Atmospheres*, *102*(D14), 17069-17079.
32. Shenk, W. E., & Curran, R. J. (1974). The detection of dust storms over land and water with satellite visible and infrared measurements. *Monthly Weather Review*, *102*(12), 830-837.
33. Takashima, T., & Masuda, K. (1987). Emissivities of quartz and Sahara dust powders in the infrared region (7–17 μ). *Remote Sensing of Environment*, *23*(1), 51-63.
34. Takashima, T., & Masuda, K. (1988). Averaged emissivities of quartz and sahara dust powders in the infrared region. *Remote Sensing of Environment*, *26*(3), 301-302.
35. King, M. D., Menzel, W. P., Kaufman, Y. J., Tanré, D., Gao, B. C., Platnick, S., ... & Hubanks, P. A. (2003). Cloud and aerosol properties, precipitable water, and profiles of temperature and water vapor from MODIS. *IEEE Transactions on Geoscience and Remote Sensing*, *41*(2), 442-458.
36. Gu, Y., Rose, W. I., & Bluth, G. J. (2003). Retrieval of mass and sizes of particles in sandstorms using two MODIS IR bands: A case study of April 7, 2001 sandstorm in China. *Geophysical Research Letters*, *30*(15).
37. Salisbury, J. W., & Wald, A. (1992). The role of volume scattering in reducing spectral contrast of reststrahlen bands in spectra of powdered minerals. *Icarus*, *96*(1), 121-128.
38. Wald, A. E., & Salisbury, J. W. (1995). Thermal infrared directional emissivity of powdered quartz. *Journal of Geophysical Research: Solid Earth*, *100*(B12), 24665-24675.
39. Wenrich, M. L., & Christensen, P. R. (1996). Optical constants of minerals derived from emission spectroscopy: Application to quartz. *Journal of Geophysical Research: Solid Earth*, *101*(B7), 15921-15931.
40. Wald, A. E., Kaufman, Y. J., Tanré, D., & Gao, B. C. (1998). Daytime and nighttime detection of mineral dust over desert using infrared spectral contrast. *Journal of Geophysical Research: Atmospheres*, *103*(D24), 32307-32313.
41. Sokolik, I. N. (2002). The spectral radiative signature of wind-blown mineral dust: Implications for remote sensing in the thermal IR region. *Geophysical Research Letters*, *29*(24), 7-1.
42. Park, S. U., & Lee, E. H. (2004). Parameterization of Asian dust (Hwangsa) particle-size distributions for use in dust emission models. *Atmospheric Environment*, *38*(14), 2155-2162.
43. Hansell, R. A., Ou, S. C., Liou, K. N., Roskovensky, J. K., Tsay, S. C., Hsu, C., & Ji, Q. (2007). Simultaneous detection/separation of mineral dust and cirrus clouds using MODIS thermal infrared window data. *Geophysical Research Letters*, *34*(11).
44. Zhang, P., Lu, N. M., Hu, X. Q., & Dong, C. H. (2006). Identification and physical retrieval of dust storm using three MODIS thermal IR channels. *Global and Planetary Change*, *52*(1-4), 197-206.

45. Orofino, V., Blanco, A., Fonti, S., Proce, R., & Rotundi, A. (1998). The infrared optical constants of limestone particles and implications for the search of carbonates on Mars. *Planetary and Space Science*, *46*(11-12), 1659-1669.
46. Marra, A. C., Blanco, A., Fonti, S., Jurewicz, A., & Orofino, V. (2005). Fine hematite particles of Martian interest: Absorption spectra and optical constants. In *Journal of Physics: Conference Series* (Vol. 6, No. 1, p. 013). IOP Publishing.
47. Stamnes, K., Tsay, S. C., Wiscombe, W., & Jayaweera, K. (1988). Numerically stable algorithm for discrete-ordinate-method radiative transfer in multiple scattering and emitting layered media. *Applied Optics*, *27*(12), 2502-2509.
48. Ricchiazzi, P., Yang, S., Gautier, C., & Sowle, D. (1998). SBDART: A research and teaching software tool for plane-parallel radiative transfer in the Earth's atmosphere. *Bulletin of the American Meteorological Society*, *79*(10), 2101-2114.
49. Mayer, B., & Kylling, A. (2005). The libRadtran software package for radiative transfer calculations-description and examples of use. Atmospheric Chemistry and Physics, 5(7), 1855-1877.
50. Pavolonis, M. and J. Sieglaff, 2009: GOES-R Advanced Baseline Imager (ABI) Algorithm Theoretical Basis Document for Volcanic Ash (Detection and Height). Available at http://www.star.nesdis.noaa.gov/goesr/docs/ATBD/VolAs h.pdf
51. Kidder, S. Q., & Jones, A. S. (2007). A blended satellite total precipitable water product for operational forecasting. *Journal of Atmospheric and Oceanic Technology*, *24*(1), 74-81.
52. He, L., Wang, L., Lin, A., Zhang, M., Bilal, M., & Wei, J. (2018). Performance of the NPP-VIIRS and Aqua-MODIS aerosol optical depth products over the Yangtze River Basin. *Remote Sensing*, *10*(1), 117.
53. Zhang, H., Kondragunta, S., Laszlo, I., & Zhou, M. (2020). Improving GOES Advanced Baseline Imager (ABI) aerosol optical depth (AOD) retrievals using an empirical bias correction algorithm. *Atmospheric Measurement Techniques*, *13*(11), 5955-5975.
54. Benedetti, A., Di Giuseppe, F., Jones, L., Peuch, V. H., Rémy, S., & Zhang, X. (2019). The value of satellite observations in the analysis and short-range prediction of Asian dust. *Atmospheric Chemistry and Physics*, *19*(2), 987-998.
55. Cao, J., Lee, S., Zheng, X., Ho, K., Zhang, X., Guo, H., ... & Wang, H. (2003). Characterization of dust storms to Hong Kong in April 1998. *Water, Air and Soil Pollution: Focus*, *3*(2), 213-229.
56. Peyridieu, S., Chédin, A., Tanré, D., Capelle, V., Pierangelo, C., Lamquin, N., & Armante, R. (2010). Saharan dust infrared optical depth and altitude retrieved from AIRS: a focus over North Atlantic–comparison to MODIS and CALIPSO. *Atmospheric Chemistry and Physics*, *10*(4), 1953-1967.